Check for updates

Geochemistry, Geophysics, Geosystems®

RESEARCH ARTICLE
10.1029/2026GC013384

Key Points:

- Carbonate-bearing breccias record transient fault-valve behavior in Alpine mid-crustal shear zones
- CO_2-bearing metamorphic fluids promoted localized embrittlement and episodic permeability during ductile deformation
- Mid-crustal breccias provide potential fossil analogs of CO_2-driven seismicity and transient fluid pathways in collisional orogens

Supporting Information:

Supporting Information may be found in the online version of this article.

Correspondence to:

A. Ceccato,
alberto.ceccato@unifi.it

Citation:

Ceccato, A., Tavazzani, L., Malaspina, N., Behr, W. M., & Bernasconi, S. M. (2026). Carbonate-bearing breccias in viscous shear zones: A fossil record of CO_2-driven transient embrittlement and enhanced permeability in the middle crust. *Geochemistry, Geophysics, Geosystems*, *27*, e2026GC013384. https://doi.org/10.1029/2026GC013384

Received 3 SEP 2026
Accepted 5 NOV 2026

Author Contributions:

Conceptualization: Alberto Ceccato, Lorenzo Tavazzani
Data curation: Alberto Ceccato, Lorenzo Tavazzani, Nadia Malaspina
Formal analysis: Alberto Ceccato, Lorenzo Tavazzani, Whitney M. Behr, Stefano M. Bernasconi
Funding acquisition: Alberto Ceccato, Nadia Malaspina
Investigation: Alberto Ceccato, Lorenzo Tavazzani, Nadia Malaspina, Whitney M. Behr

© 2026 The Author(s). Geochemistry, Geophysics, Geosystems published by Wiley Periodicals LLC on behalf of American Geophysical Union.
This is an open access article under the terms of the Creative Commons Attribution License, which permits use, distribution and reproduction in any medium, provided the original work is properly cited.

Carbonate-Bearing Breccias in Viscous Shear Zones: A Fossil Record of CO_2-Driven Transient Embrittlement and Enhanced Permeability in the Middle Crust

Alberto Ceccato[1,2], Lorenzo Tavazzani[3], Nadia Malaspina[4], Whitney M. Behr[1], and Stefano M. Bernasconi[1]

[1]Department of Earth and Planetary Sciences, Geological Institute, Zurich, Switzerland, [2]Dipartimento di Scienze della Terra, Università di Firenze, Firenze, Italy, [3]Department of Earth and Planetary Sciences, Institute of Geochemistry and Petrology, Zurich, Switzerland, [4]Department of Earth and Environmental Sciences, University of Milano-Bicocca, Milano, Italy

Abstract Earthquakes and surficial emissions of carbon dioxide (CO_2) are currently observed along collisional orogens worldwide; however, direct geological evidence linking mid-crustal CO_2 transfer to transient seismic deformation remains scarce. Here we document carbonate-bearing breccias and fault veins preserved within Alpine mid-crustal shear zones that record brittle deformation and fluid flow under supra-lithostatic (>500 MPa) fluid pressures. Structural observations, C-O-Sr isotope systematics, trace-element data, and calcite solubility modelling indicate that these structures were formed by fault-valve processes, where transient dilatancy triggered carbonate precipitation from low-salinity H_2O–CO_2 metamorphic fluids. The localized occurrence of carbonate-bearing breccias within otherwise ductile hydrous shear zones suggests that CO_2-bearing fluids may promote transient embrittlement and permeability enhancement under conditions where distributed viscous deformation would normally dominate. Modelling demonstrates that carbonate precipitation during a single dilatancy-related pressure drop has limited sealing efficiency (<0.05% of the dilatant volume), hinting at the occurrence of past sustained permeability and fluid flow to explain the large carbonate volumes preserved in the field. These structures provide a fossil analogue for fluid overpressure and aftershock-related permeability pulses beneath active collisional orogens such as the Himalaya, suggesting that carbon-driven hydrofracturing can indeed operate through fault-valve behavior to regulate episodic permeability and carbon transport in the middle crust.

Plain Language Summary Carbon dioxide (CO_2) is released from deep rocks during mountain building, but how it moves through the Earth's crust, and how its flux is related to deformation is still poorly understood. In particular, it is unclear how CO_2-bearing fluids migrate through the middle crust, where rocks are generally expected to deform by flowing rather than by breaking. In this study, we examine rocks from the European Alps that preserve evidence of past fluid flow along deep fault-related shear zones. We found that CO_2-bearing fluids moved through the crust in short-lived pulses, triggered when high fluid pressures caused rocks to fracture suddenly, creating temporary pathways for fluid flow. As pressure dropped during these events, minerals such as calcite precipitated and partially sealed fractures. However, our results show that this sealing process is very inefficient. This means that either fractures opened and sealed repeatedly or fluids continued to flow through partially open pathways. This behavior suggests that the middle crust can become temporarily permeable during deformation, allowing CO_2 to move upward in bursts. These findings provide field-based evidence that CO_2 can help drive rock fracturing at depth, offering a geological example of processes that may occur beneath active mountain belts, where fluid pressure and small earthquakes are closely linked.

1. Introduction

Surface emissions of carbon-dioxide (CO_2) of different origins (magmatic, metamorphic, mantle) correlate with both deep and shallow seismicity along tectonic margins (Irwin & Barnes, 1980; Lee et al., 2016; Liu et al., 2024; Tamburello et al., 2018). In active collisional belts such as the Himalayas, earthquake hypocenters often overlie high-conductivity domains (Lemonnier et al., 1999; Rawat et al., 2014) inferred to be linked to metamorphic fluids released by mid- to lower-crustal devolatilization reactions (Evans et al., 2008; Groppo et al., 2022). Upward advection of CO_2-*rich* fluids is expected to occur along *deep* seismogenic faults connecting the lower lithosphere to the surface of the Earth (Frezzotti et al., 2009; Groppo et al., 2022; Lee et al., 2016; Malusà

Methodology: Alberto Ceccato, Lorenzo Tavazzani, Whitney M. Behr, Stefano M. Bernasconi
Project administration: Alberto Ceccato
Resources: Alberto Ceccato, Nadia Malaspina, Whitney M. Behr
Software: Alberto Ceccato
Supervision: Whitney M. Behr
Validation: Alberto Ceccato, Lorenzo Tavazzani, Nadia Malaspina, Whitney M. Behr, Stefano M. Bernasconi
Visualization: Alberto Ceccato, Lorenzo Tavazzani
Writing – original draft: Alberto Ceccato
Writing – review & editing: Alberto Ceccato, Lorenzo Tavazzani, Nadia Malaspina, Whitney M. Behr, Stefano M. Bernasconi

et al., 2022; Tamburello et al., 2018). In quartz-rich rocks, CO_2-*rich* fluid migration is inefficient, requiring the development of localized structural permeability induced by fluid overpressure and hydrofracturing (carbo-fracturing; Brenan & Watson, 1988; Giuntoli et al., 2024; Groppo et al., 2022; Holness, 1992; Watson & Brenan, 1987). Indeed, at shallow crustal conditions, *overpressured* CO_2-*rich* fluids are inferred to promote *fault-valving* processes (i.e., recurrent seismic faulting induced by transient high fluid pressure, followed by permeability enhancement, fluid flow, mineral precipitation, and fault sealing; Sibson, 1990; Miller et al., 2004; Collettini et al., 2008). Conversely, at mid-to-lower-crustal conditions, *deep* faults are generally expected to accommodate deformation by ductile creep—aided by H_2O-driven metamorphic reactions (e.g., Oliot et al., 2014)—and channeling fluids through grain-scale dynamic pore networks (Fusseis et al., 2009). Direct geological evidence and possible mechanisms linking meso-to-large scale CO_2-*rich* fluid transport to transient, potentially seismic deformation at these conditions remains scarce (e.g., Groppo et al., 2022). In this framework, two key questions remain unanswered: (a) are there any meso-scale structural features in orogenic settings documenting a close relationship between transient deformation and CO_2-*rich* fluid transport? (b) If so, how *rich* are the CO_2-*bearing* fluids in such a context?

Here, we investigate carbonate-bearing breccias and fault-veins preserved within a regional network of ductile shear zones in the Central and Western European Alps, recording fault-valving at >350°C–400°C and 0.5–0.8 GPa and carbonate precipitation from low-salinity H_2O-CO_2 metamorphic fluids. Using carbonates as a proxy for past flow of CO_2-bearing fluids in an otherwise carbonate-free host rock, we demonstrate that these carbonate-bearing breccias represent a potential fossil analogue for coupled deformation, permeability generation, and metamorphic CO_2 transfer at mid-crustal conditions. Specifically, we present field and microstructural characteristics, $\delta^{13}C$, $\delta^{18}O$, and $^{87}Sr/^{86}Sr$ systematics, calcite solubility modelling, along with literature data review to constrain: (a) the potential origin of the fluid (Section 4.1); (b) the chemo-mechanical feedback between deformation at CO_2-present conditions, carbonate precipitation, and mid-crustal permeability dynamics (Sections 4.2–4.4); (c) the regional context and location of carbonate-bearing breccias in the Central Alps, to define their role in the orogen-scale plumbing system (Section 4.5) and carbon cycle (Section 4.6).

The Central and Western European Alps provide a natural laboratory to investigate how tectonic mid-crustal deformation interacts with metamorphic fluid transfer in collisional orogens. The more internal Penninic units structurally overlie the External Crystalline Massifs (ECMs), both representing the former European crystalline basement recording collisional shortening under low-greenschist- to high-amphibolite-facies conditions (Figure 1a; Text S1 in Supporting Information S1; Ceccato et al., 2024; Todd & Engi, 1997). The outermost Alpine domains are formed by the Helvetic units, consisting of low-grade metasedimentary nappes that were detached from both the internal Penninic and the ECMs along major regional thrusts, namely the Penninic Frontal Thrust and the Glarus Thrust (Figure 1a). A regional-scale advective fluid flow system connecting the internal Penninic units to major Helvetic thrusts has been defined based on geochemical and C-O-Sr isotopic trends of carbonate minerals in syn-kinematic tectonic veins (Badertscher, Abart, et al., 2002; Badertscher, Beaudoin, et al., 2002; Burkhard & Kerrich, 1988; Burkhard et al., 1992; Cardello et al., 2024; Dietrich et al., 1983; Hoefs & Stalder, 1977; Kirschner et al., 1995, 1999; Marquer et al., 1994; Mullis et al., 1994; Sharp, 2005; Tarantola et al., 2007). Potential relationship between cyclic seismic activity and fluid flow has been speculatively proposed for such systems (Badertscher & Burkhard, 2002). Within the ECMs, polymetamorphic basement rocks are crosscut by a dense network of retrograde Alpine-age ductile shear zones, associated with pervasive metamorphic fluid flow and H_2O-driven metamorphic reactions (Ceccato et al., 2022, 2024; Goncalves et al., 2012; Guermani & Pennacchioni, 1998; Marquer & Burkhard, 1992; Oliot et al., 2014; Rolland & Rossi, 2016; Rossi & Rolland, 2014), and extensional veining ("Alpine-type" quartz + feldspar + chlorite + calcite veins; Heijboer, 2006; Hoefs & Stalder, 1977; Mullis et al., 1994; Rossi & Rolland, 2014; Sharp, 2005; Tarantola et al., 2007). Large calcite single crystals and carbonate-bearing mineralization are commonly reported from such extensional veins and shear zones (e.g., Cesare et al., 2001; Rolland et al., 2008; Rolland & Rossi, 2016; Rossi & Rolland, 2014). It is within these shear zones that we document large volumes of previously unreported carbonate-bearing breccias and fault veins that provide new insights into the relationships between deformation and CO_2-bearing fluid flow at mid-crustal conditions.

15252027, 2026, 11, Downloaded from https://agupubs.onlinelibrary.wiley.com/doi/10.1029/2026GC013384 by CochraneItalia, Wiley Online Library on [17/11/2026]. See the Terms and Conditions (https://onlinelibrary.wiley.com/terms-and-conditions) on Wiley Online Library for rules of use; OA articles are governed by the applicable Creative Commons License

10.1029/2026GC013384

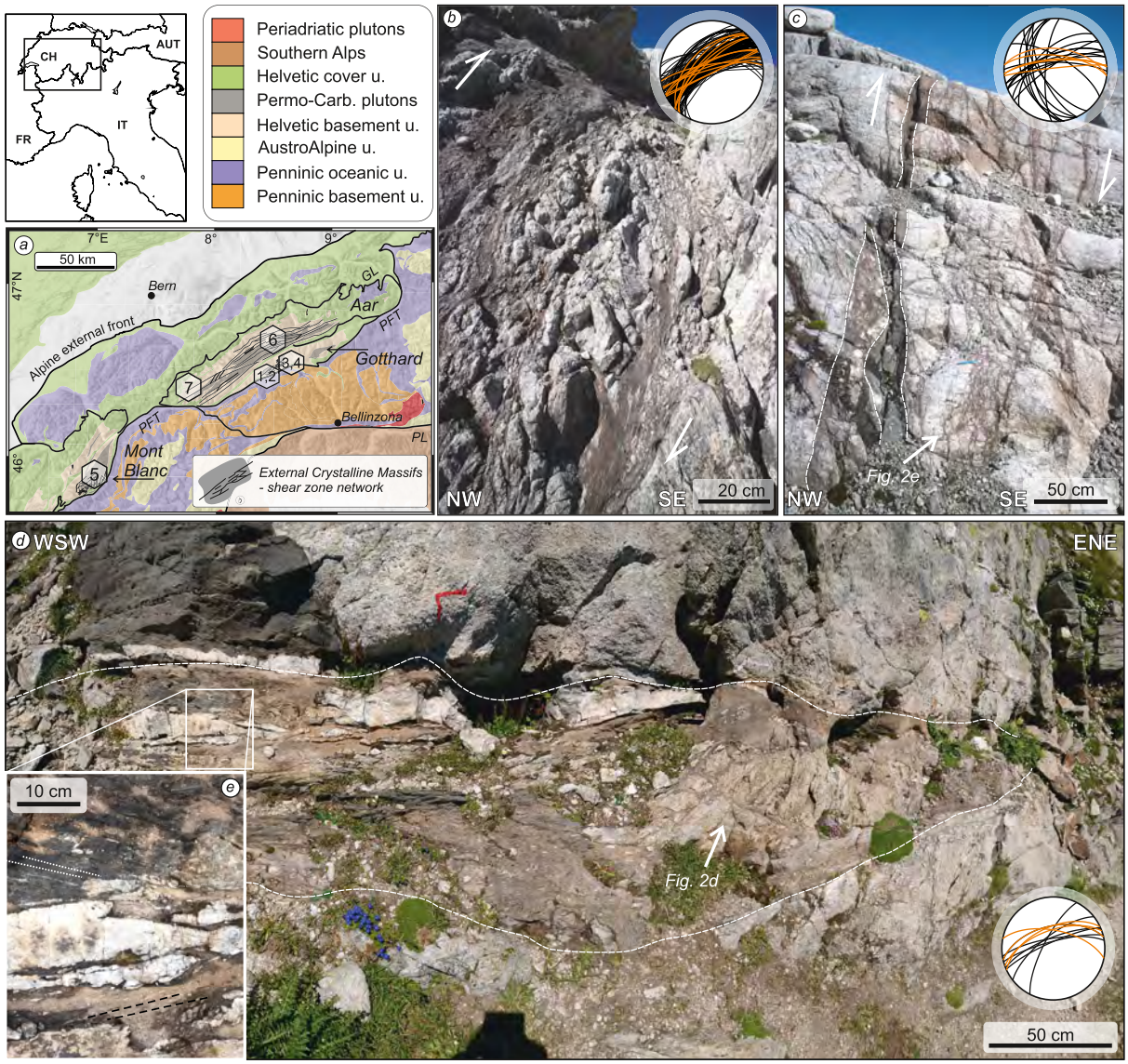


Figure 1. Carbonate-bearing breccias in Alpine shear zones of the External Crystalline Massifs. (a) Schematic geological map of the Western and Central Alps, showing the location of the External Crystalline Massifs, the shear zone network (Ceccato et al., 2024; Piantelli et al., 2026; Rolland et al., 2008), and the studied outcrops (Gotthard: 1–2 Rotondo; 3–4 Fibbia-Lucendro; Mont Blanc: 5 Toula; Aar: 6 Voralptal; 7 Lötschepass). *PL*, Periadriatic lineament; *PFT*, Penninic Frontal Thrust; *GL*: Glarus thrust. Background hillshaded digital terrain model from Nasa SRTM database. (b) Sheared carbonate-bearing breccia from Gotthard (Rotondo, 1, 2), vertical outcrop showing top-to-southeast reverse shearing of the breccia. (c) Carbonate-bearing breccias adjacent to a reverse shear zone in the Mont Blanc (Toula glacier outcrops), vertical outcrop. (d) Sheared carbonate-bearing breccias and cataclasites from Gotthard (Passo di Lucendro 3, 4), horizontal outcrop, panorama view from above. (e) Magnification of (d) showing clasts of foliated mafic dyke (dotted lines) included in a sheared carbonate-bearing breccia (black dashed lines define the foliation). The stereoplot insets show the orientation of the major shear zones in the areas (black great circles) and of the major carbonate-bearing structures (orange great circles—Original data and data set from Ceccato et al. (2024).

2. Materials and Methods

2.1. Field Structural Analyses and Lineament Mapping

Structural analyses of shear zone occurrences, orientation and geometry were performed in the field. Remote sensing analyses aimed at the identification of the large-scale geometry and pattern of fault/shear zone network were performed on hillshaded digital terrain models from different sources (see Supporting Information S1), as well as orthomosaics of analyzed outcrops. Orthomosaics were produced from drone surveys. Drone surveys were acquired using a DJI Mavic 2 pro aircraft equipped with a Hasselblad L1D-20C aerial camera, with an effective resolution of 20 MP. Drone flights were conducted in manual mode at a constant altitude above the outcrops with

15252027, 2026, 11, Downloaded from https://agupubs.onlinelibrary.wiley.com/doi/10.1029/2026GC013384 by CochraneItalia, Wiley Online Library on [17/11/2026]. See the Terms and Conditions (https://onlinelibrary.wiley.com/terms-and-conditions) on Wiley Online Library for rules of use; OA articles are governed by the applicable Creative Commons License

15252027, 2026, 11, Downloaded from https://agupubs.onlinelibrary.wiley.com/doi/10.1029/2026GC013384 by CochraneItalia, Wiley Online Library on [17/11/2026]. See the Terms and Conditions (https://onlinelibrary.wiley.com/terms-and-conditions) on Wiley Online Library for rules of use; OA articles are governed by the applicable Creative Commons License

the camera oriented perpendicularly to the surface, as well as at 45 and 30° inclination angles. The images were processed using Agisoft Metashape 1.8.4 (64-bit) software to generate a 2.5D model, and the corresponding orthoimages. Maps and geological sketches were elaborated using ArcGIS Pro 3.4.0, and figures were prepared using CorelDRAW 2021.

2.2. Optical and Scanning Electron Microscopy

Petrographical analyses were performed on oriented thin sections of selected samples, cut parallel to the lineation and perpendicular to the foliation/shear plane. Backscattered electron (BSE) images and Energy Dispersion Spectrometry for phase identification were performed at ScopeM (ETH) with Hitachi SU5000 SEM. Analytical conditions are indicated at the bottom of BSE images in the main text.

2.3. Carbon and Oxygen Stable Isotopes

Carbonate powders were obtained through microdrilling of hand samples using a 1.5 mm drill bit. The C and O stable isotope quantification of the selected powdered samples was performed at the Stable isotope Laboratory at ETH Zurich using a Thermo Fisher Delta V with GasBench II carbonate preparation device following (Breitenbach & Bernasconi, 2011). Every 10 samples, the standards MS2 and IsoB were analyzed. Carbon isotope composition is reported in the δ notation as $\delta^{13}C$ with respect to Vienna Pee Dee Belemnite (V-PDB); oxygen isotope composition is reported in δ notation as $\delta^{18}O$ with respect to Vienna Standard Mean Ocean Water (V-SMOW). Data are reported in DR1 in Supporting Information S1.

In situ trace element analyses of carbonates were performed by LA-ICP-MS at ETH Zürich using an ASI RESOlution-LR excimer (ArF, 193 nm) laser ablation system coupled to a Thermo Element XR sector-field ICP-MS. The synthetic glass standard NIST SRM612 was used as a primary reference material, while USGS GSD-1G glass (Guillong et al., 2005) and NIST SRM610 glass (Jochum et al., 2011) were analyzed together with carbonate reference material WC-1 (Roberts et al., 2017) during each session to check accuracy and reproducibility. A 43 µm spot size and 4 Hz repetition rate with a laser energy density on the sample surface of ca. 2 J/cm were used for ablation of unknowns and reference materials. The ablation aerosol was mixed in the fast washout S-155 ablation cell (Laurin Technic) with carrier gas consisting of helium (ca. 0.25 L/min) and make-up gas consisting of argon (ca. 1 L/min) and nitrogen (2 mL/min). The ablated aerosol was then homogenized by flushing through a squid device before introduction into the plasma torch. The single collector sector-field MS is equipped with a high-capacity (80 m^3/hr) interface pump to improve the sensitivity. Before each analytical session the instrument is optimized on NIST SRM612 glass to achieve a detection efficiency in the range of 1% (on Pb, Th, U) while keeping a low oxides production ($^{248}ThO^+/^{232}Th^+ \leq 0.25\%$) and the U/Th ratio of ca. 1. Intensities are recorded for the following isotopes: ^{23}Na, ^{24}Mg, ^{27}Al, ^{29}Si, ^{39}K, ^{43}Ca, ^{45}Sc, ^{49}Ti, ^{51}V, ^{53}Cr, ^{55}Mn, ^{57}Fe, ^{59}Co, ^{60}Ni, ^{65}Cu, ^{66}Zn, ^{85}Rb, ^{88}Sr, ^{89}Y, ^{90}Zr, ^{93}Nb, ^{95}Mo, ^{133}Cs, ^{137}Ba, ^{139}La, ^{140}Ce, ^{141}Pr, ^{146}Nd, ^{147}Sm, ^{151}Eu, ^{157}Gd, ^{159}Tb, ^{163}Dy, ^{165}Ho, ^{167}Er, ^{169}Tm, ^{173}Yb, ^{175}Lu, ^{178}Hf, ^{181}Ta, ^{208}Pb, ^{232}Th, ^{238}U. The resulting raw intensities were processed offline with Iolite4 software (Paton et al., 2011) using the "Trace Elements" data reduction scheme. CaO concentrations of 30.41 wt% and 56.03 wt% were used as internal standard for relative sensitivity correction of dolomite and calcite materials, respectively. Detailed instrumentation and data acquisition parameters together with the complete trace elements data set for samples and validation reference materials are reported in Table S2.

In situ Sr isotope analyses of vein carbonates were undertaken on an ASI RESOlution-SE excimer (ArF, 193 nm) laser ablation system interfaced to a Nu Plasma II MC-ICP-MS at ETH Zürich and following a similar approach to that of Fitzpayne et al. (2023) and Tavazzani et al. (2024). Analytical conditions included 38–100 µm spot size, a repetition rate of 5–10 Hz, and laser fluence of ∼2.5–3.5 J/cm^2 depending on the Sr mass fraction for the analyzed material. Each analysis consisted of a sequence of 30 s of gas blank measurement, 30 s of ablation and 10–30 s of washout. Total Sr signal intensities varied widely (up to ∼4 V) in analyzed carbonates, but only analyses with yield >0.5 V were retained. Data reduction, including corrections for isobaric interferences (Kr, Ca dimers, Ca argides) instrumental mass bias was performed in Iolite4 (Paton et al., 2007, 2011) using the Sr Isotopes Universal data reduction scheme (Mulder et al., 2023). Instrumental drift was evaluated by repeated measurement of Modern Marine Carbonate (MMC), which was ablated together with the ADP-09 dolomite (ADP-9; solution-mode $^{87}Sr/^{86}Sr = 0.707945 \pm 0.000017$) and Oka carbonate (OKA; solution-mode $^{87}Sr/^{86}Sr = 0.703253 \pm 0.000005$) for every block of 11 unknowns. The data are reported relative to MMC $^{87}Sr/^{86}Sr$ of 0.709163 (Woodhead

15252027, 2026, 11, Downloaded from https://agupubs.onlinelibrary.wiley.com/doi/10.1029/2026GC013384 by CochraneItalia, Wiley Online Library on [17/11/2026]. See the Terms and Conditions (https://onlinelibrary.wiley.com/terms-and-conditions) on Wiley Online Library for rules of use; OA articles are governed by the applicable Creative Commons License

et al., 2005) via standard bracketing. Weighted mean $^{87}Sr/^{86}Sr$ for Oka (0.70325 ± 11, n = 20) and ADP-09 (0.70795 ± 31, n = 13/20) are consistent with the solution-mode values. $^{84}Sr/^{86}Sr$ of MMC, OKA and Sr-rich carbonate unknowns are generally within uncertainty of the natural ratio (~0.0565). Marginally lower or higher values for this ratio can stem from low counting statistics for ^{84}Sr for Sr-poor carbonates and/or overestimation of CaAr isobaric interference at mass 84. Although this effect has a negligible role on quantification of ^{86}Sr and ^{87}Sr, and $^{84}Sr/^{86}Sr$ is indeed not correlated with $^{87}Sr/^{86}Sr$ in our data set (not shown), we have excluded measurements with $^{84}Sr/^{86}Sr$ values outside of the $0.0550 < {}^{84}Sr/^{86}Sr < 0.590$ interval. $^{87}Rb/^{86}Sr$ ratios are negligible for most analyzed carbonates (i.e., <0.001), which makes corrections for ^{87}Sr ingrowth insignificant. Therefore, the reported Sr isotope ratios are equal to the initial Sr isotope ratios at the time of carbonate crystallization. Only one sample (MB14A) yielded analyses with substantially higher Rb contents; for this specific sample, we retained only analyses with $^{87}Rb/^{86}Sr < 0.05$ as suggested by Irrgeher et al. (2016) and Mulder et al. (2023). The complete Sr isotope data set, including carbonate unknowns and reference materials, is reported in Table S3.

2.3.1. Carbonate Solubility Modelling

We adopt the calcite solubility model of Caciagli & Manning (2003) and the equation of state for H_2O of Pitzer and Sterner (1995) to compute (a) calcite molality in the desired pressure-temperature space and (b) the variation of calcite solubility due to fluid pressure drops in fractures and fault zones. Calcite molality (m_{CaCO_3}) expressed as mol of solute $CaCO_3$ per kg of pure H_2O at variable pressure (P) and temperature (T) conditions is given by the equation:

$$\mathrm{Log}_{10}\left(m_{\mathrm{CaCO_3}}\right) = -3.95 + 0.00266\ T + (32.8 - 0.028\ T)\ \mathrm{Log}_{10}\left(\rho_{\mathrm{H20}}\right)$$

ρ_{H_2}o represents the density of pure H_2O as a function of temperature and pressure conditions, as described by the equations of state presented by Pitzer & Sterner (1995). With a quantitative approach similar to Williams (2019), we calculate the maximum sealing efficiency considering for each P-T condition the total volume of calcite dissolved in the fluid (V_{CaCO_3}), divided by the available fluid volume

$$\eta_S\ (\%) = V_{\mathrm{Calcite}}/V_{\mathrm{Fluid}}\ \cdot 100 = m_{\mathrm{CaCO3}} \cdot \rho_{\mathrm{CaCO3}}/V_{\mathrm{Fluid}} \cdot 100$$

The P-T diagrams in Figure 6 have been computed by integrating the equations in a Matlab© script (see Supporting Information S1 and data repository).

3. Data and Results

3.1. Field Relationships and Microstructures

In the ECMs, Alpine shear zones locally host large volumes of carbonate-bearing cataclasites, breccias, and quartz-calcite fault-veins (Figures 1 and 2, Figures S1–S3 in Supporting Information S1). Field and microstructural relationships document repeated episodes of brittle fracturing followed by mineral precipitation and overprinting within Alpine shear zones, from prograde to retrograde metamorphic conditions (Texts S1 and S2 in Supporting Information S1). Carbonate-bearing structures are observed to overprint both *pre-existing*, potentially pre-Alpine faults (Figures 1c and 2a–2e), Alpine-age foliated shear zones (Figures 1d and 2d), and locally record ductile transposition at high-temperature (Figures 1b–1d). They occur both as pristine, carbonate-impregnated fault rocks (Figures 2a and 3a), and as recrystallized breccias and veins embedded within ductile shear zones (Figures 1b and 3d). Carbonate structures are up to m-thick, continuous over several meters, and observed discontinuously over the entire along-strike exposure of analyzed shear zones, adding up to tens of m^2 of exposed carbonate surface (up to 10% of the exposed shear zone area; see Figure S1, Text S4 in Supporting Information S1). Along the main shear planes, multiple quartz-calcite fault-veins are observed: cm-wide fault-veins present lattice-bladed calcite texture (Figures 3a and 3b), whereas mm-scale alternation of calcite and host rock layers compose laminated fault-veins (Figure 2c). Fault-veins display lineated surfaces, suggesting post-veining shear deformation (Figure 2b). Breccias commonly occur as selvages along main shear planes and at fault jogs (Figures 1c and 2f; Figures S3d–S3f in Supporting Information S1). Mosaic-, crackle- to chaotic-breccias consist of angular granite clasts suspended in a blocky carbonate (rhombohedral calcite or saddle dolomite) cement precipitated in open spaces (Figures 2d and 2e). Breccia bodies also form mm-to-cm wide injection-like veins at high-angle to the main shear plane (Figures 2e and 3d). Carbonate-bearing cataclasites and calcite-quartz veins

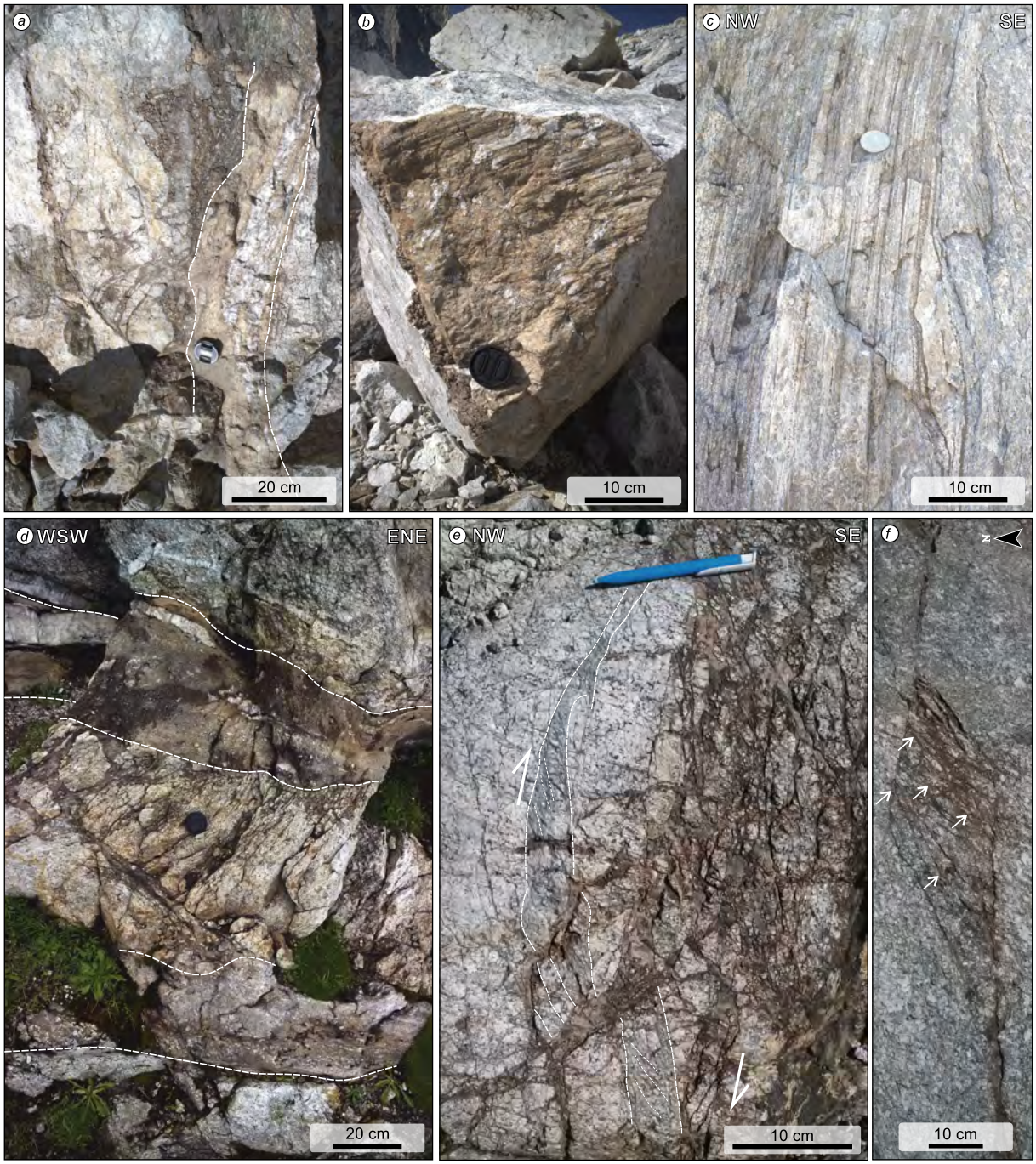


Figure 2. Details of carbonate-bearing faults and shear zones in the field. (a) Crosscutting relationship between a carbonated cataclasite and a quartz-calcite fault-vein (delimited by dashed curves) in the Gotthard (Passo di Rotondo, loose boulder). (b) Lineated quartz-calcite fault-vein surface at Passo di Rotondo; loose boulder. (c) Finely banded quartz-calcite mylonite overprinting laminated calcite fault veins at the Rotondo outcrop, vertical outcrop cutting across the shear zone parallel to dip and perpendicular to strike. (d) Different carbonate-bearing layers in a major shear zone in the Gotthard (Passo di Lucendro), including from bottom to top: sheared cataclasite, carbonate-bearing breccia, quartz-calcite fault-vein; see outcrop orientation in Figure 1d. (e) Carbonate-bearing breccia in the Mont Blanc (Toula glacier outcrops) cutting across an Alpine greenschist shear zone (Guermani & Pennacchioni, 1998) recording dilation and reverse shearing (consistent with the shear zone kinematics). (f) Carbonate infilling (white arrows) in a dilational jog in the reactivated *pre-exiting* faults of the Mont Blanc—map view on a flat outcrop.

contain calcite + epidote + feldspar + muscovite/biotite assemblages (Figure 3b), whereas banded mylonites present recrystallized calcite + phlogopite + Mg-actinolite ± feldspars (Figures 3d and 3e), or dynamically recrystallized calcite (Figure 3f). Mineral assemblages and dynamic recrystallization indicate minimum

15252027, 2026, 11, Downloaded from https://agupubs.onlinelibrary.wiley.com/doi/10.1029/2026GC013384 by CochraneItalia, Wiley Online Library on [17/11/2026]. See the Terms and Conditions (https://onlinelibrary.wiley.com/terms-and-conditions) on Wiley Online Library for rules of use; OA articles are governed by the applicable Creative Commons License

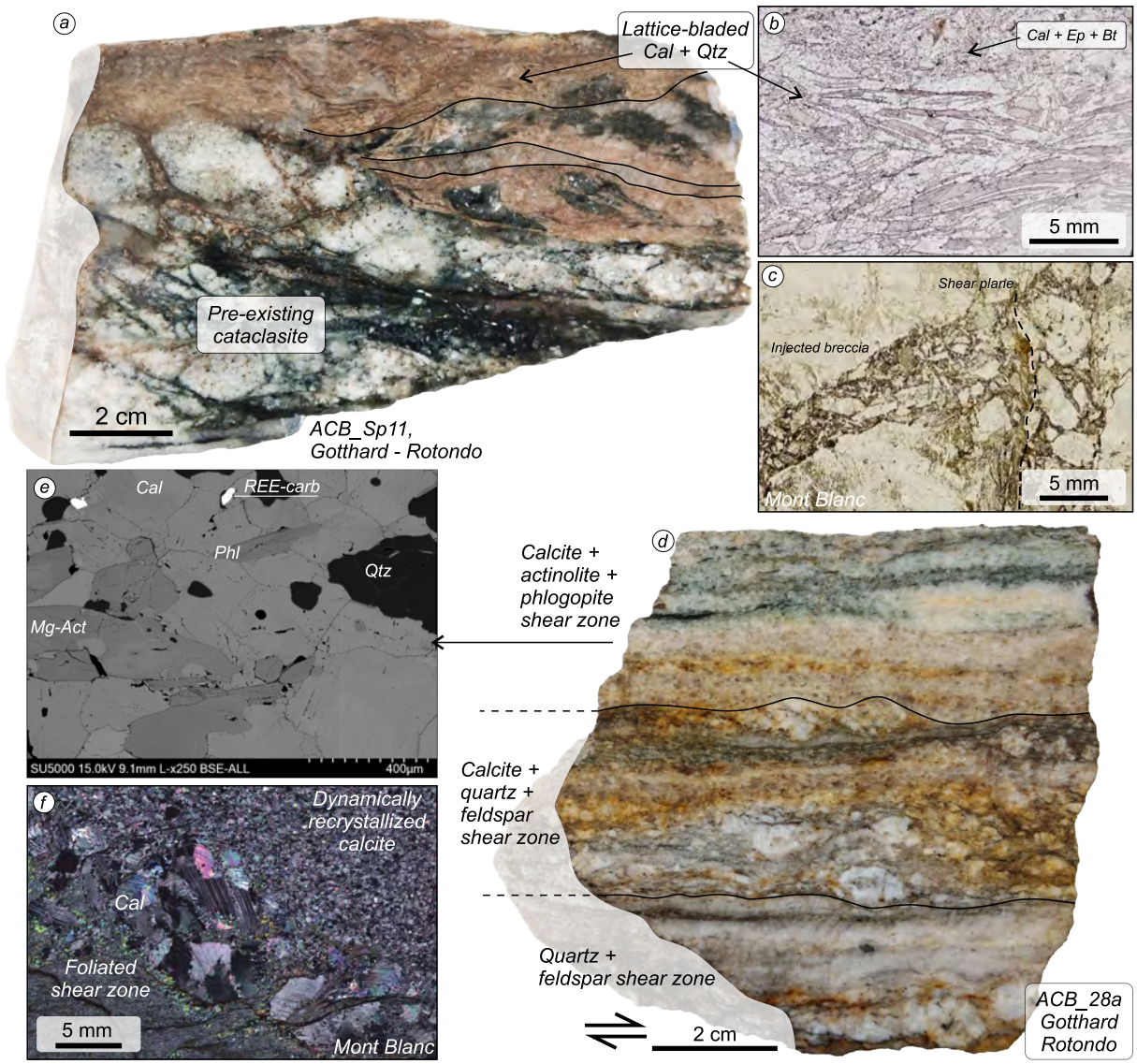


Figure 3. Hand-samples and microstructures of pristine carbonate-bearing fault-veins and ductile sheared breccias. (a) Hand-sample of *pre-existing* fault disrupted by newly formed quartz-calcite fault-vein from Gotthard outcrops—loose block, not oriented. (b) Microstructure of the cm-scale fault-vein presenting lattice-bladed calcite and quartz from the sample in (a). (c) Injection vein-like structure in the dolomite-bearing breccia from Mont Blanc. (d) Hand-sample of ductilely sheared carbonate breccia presenting a cm-scale banded texture from Gotthard outcrops, oriented sample, top-to-south reverse kinematics. (e) BSE image of the Cal + Act + Phl assemblage in the sheared carbonate breccia. (f) Layers of dynamically recrystallized calcite in the Mont Blanc shear zone from Figure 1c.

temperatures of 300°C–350°C (up to 380°C–480°C) (Ferrill et al., 2004; Meggiolaro et al., 2011; Taylor & Bucher-Nurminen, 1986) during ductile shearing, compatible with mid-crustal deformation conditions. These relationships demonstrate that carbonate formation is systematically associated with transient brittle deformation within the Alpine ductile shear zones.

3.2. C-O-Sr Isotopes and Trace Element Systematics

The large carbonate volumes (Figure 2, Figures S1 and S3 in Supporting Information S1) hosted in granitoid and felsic orthogneiss indicate an external carbon source, as these rocks contain negligible primary carbon (Rast et al., 2022). In general, carbonates display systematically depleted $\delta^{13}C$ (−8.5 to 0.3‰$_{PDB}$) and $\delta^{18}O$ (7.7–16.4‰$_{VSMOW}$; Figure 4a, Table S1). The $^{87}Sr/^{86}Sr$ values are generally highly radiogenic, ranging from 0.714 to 0.734 for the Gotthard samples, and from 0.703 to 0.737 for the Mont Blanc samples (Figure 4b, Table S3). Overall, analyzed vein carbonates show consistently steep REE patterns (i.e., normalized to Post-

15252027, 2026, 11, Downloaded from https://agupubs.onlinelibrary.wiley.com/doi/10.1029/2026GC013384 by CochraneItalia, Wiley Online Library on [17/11/2026]. See the Terms and Conditions (https://onlinelibrary.wiley.com/terms-and-conditions) on Wiley Online Library for rules of use; OA articles are governed by the applicable Creative Commons License

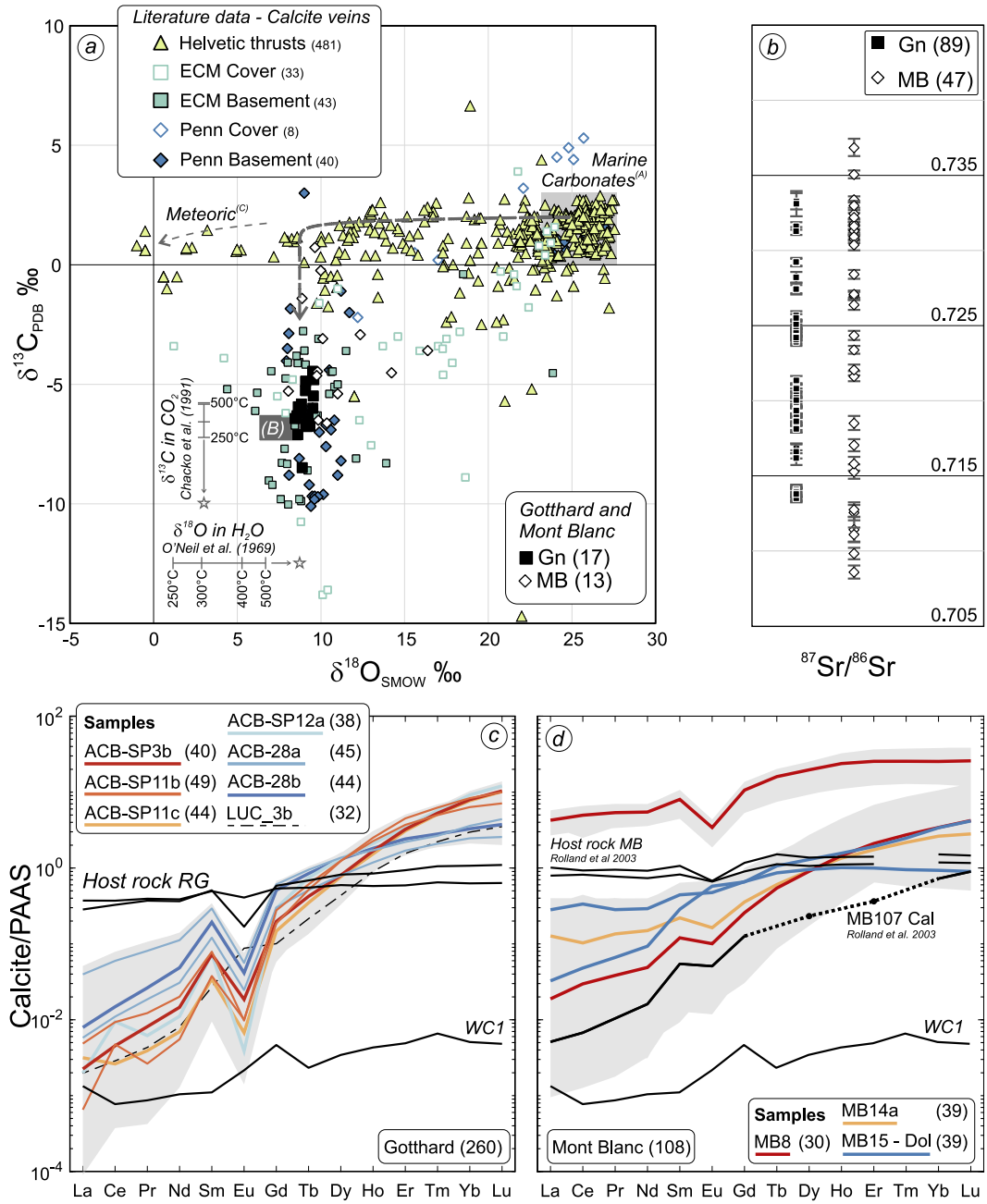


Figure 4. C-O-Sr isotopic and trace element data from carbonate-bearing breccias and fault-veins. (a) C-O stable isotope data from carbonate-bearing breccias in the Gotthard nappe (*Gn*) and Mont Blanc (*MB*). C-O stable isotope data from tectonic veins in Helvetic thrust faults (Badertscher & Burkhard, 2002; Burkhard & Kerrich, 1988; Burkhard et al., 1992; Cardello et al., 2024; Dietrich et al., 1983; Kirschner et al., 1995, 1999), Penninic (Luisier et al., 2021; Mercolli et al., 1987; Pawlig & Baumgartner, 2001; Pennacchioni et al., 2016; Sharp, 2005), and External Crystalline massifs (Heijboer, 2006; Marquer et al., 1994; Rossi & Rolland, 2014; Sharp, 2005) from the literature are also reported. Gray box (a) defines the isotopic range measured for local Helvetic carbonates (from Burkhard & Kerrich, 1988); Gray box (b) defines the isotopic range expected for metamorphic fluids from Badertscher et al. (2002a) estimated considering equilibrium isotopic fractionation between H_2O and Calcite at 300°C along the Glarus thrust (O'Neil et al., 1969); Dashed curve (c) indicate the isotopic trend of meteoric-derived carbonate veins from Cardello et al. (2024). We report the range of $\delta^{13}C$ of CO_2 computed following Chacko et al. (1991) from the lowest $\delta^{13}C$ data of the carbonate veins from the basement units (gray hollow star). Similarly, we show the expected $\delta^{18}O$ range of the parental metamorphic fluid inferred from average $\delta^{18}O$ of carbonate veins in the basement (gray hollow star; following O'Neil et al., 1969). The bold dashed curve indicates the isotopic fractionation trend defined by Badertscher and Burkhard (2002) and Kirschner et al. (1999) simulating the interaction of a low-X_{CO2} fluid with a host carbonate rock. (b) $^{87}Sr/^{86}Sr$ ratios for carbonate-bearing samples from Gotthard and Mont Blanc calcite veins. (c) Average (i.e., by sample) REE patterns normalized to Post-Archean Australian Shale (PAAS; Pourmand et al., 2012) for the carbonate samples in the Gotthard nappe shear zones. (b) Average PAAS-normalized REE patterns for the carbonate samples in the Mont Blanc shear zones. Gray areas in (c) and (d) represent the full range of individual analyses.

15252027, 2026, 11, Downloaded from https://agupubs.onlinelibrary.wiley.com/doi/10.1029/2026GC013384 by CochraneItalia, Wiley Online Library on [17/11/2026]. See the Terms and Conditions (https://onlinelibrary.wiley.com/terms-and-conditions) on Wiley Online Library for rules of use; OA articles are governed by the applicable Creative Commons License

15252027, 2026, 11, Downloaded from https://agupubs.onlinelibrary.wiley.com/doi/10.1029/2026GC013384 by CochraneItalia, Wiley Online Library on [17/11/2026]. See the Terms and Conditions (https://onlinelibrary.wiley.com/terms-and-conditions) on Wiley Online Library for rules of use; OA articles are governed by the applicable Creative Commons License

Archean Australian Shale, PAAS; Pourmand et al., 2012), characterized by depletion in LREE, enrichment in HREE and more pronounced negative Eu anomaly when compared to the granitic host rock (Figures 4c and 4d; Table S2).

4. Discussions

4.1. Carbonates From Metamorphic Fluids

Across geologic settings, carbonate material is considered a reliable proxy for the source, pathway and flux of past fluid flow events (e.g., Looser et al., 2025; Nuriel et al., 2017). In this study, we compare the results of trace element geochemistry and C-O-Sr isotope analyses with available regional data to infer the origin and composition of parental fluids involved in the precipitation of voluminous carbonate materials at mid-crustal depths (e.g., Williams et al., 2019). In Figures 4 and 5, we compare $\delta^{13}C$–$\delta^{18}O$ carbonates data with a regional compilation of carbonate-bearing tectonic veins and shear zones, and fluid inclusion compositions across the Central Alps (see regional data distribution in Figure 5a; Badertscher, Abart, et al., 2002; Burkhard & Kerrich, 1988; Burkhard et al., 1992; Cardello et al., 2024; Cesare et al., 2001; Dietrich et al., 1983; Heijboer, 2006; Hoefs & Stalder, 1977; Kirschner et al., 1995, 1999; Luisier et al., 2021; Marquer et al., 1994; Mercolli et al., 1987; Mullis et al., 1994; Pawlig & Baumgartner, 2001; Pennacchioni et al., 2016; Rossi & Rolland, 2014; Sharp, 2005; Tarantola et al., 2007). These carbonate-bearing veins are generally interpreted to precipitate from fluids resulting from metamorphic devolatilization reactions occurring at the core of the Alpine orogen (e.g., Burkhard et al., 1992; Burkhard & Kerrich, 1988; Gnos et al., 2021; Mullis et al., 1994; Rauchenstein-Martinek et al., 2016; Rossi & Rolland, 2014). The $\delta^{13}C$–$\delta^{18}O$ values are comparable to carbonates from tectonic veins in similar Penninic and External crystalline basements (Figure 4a). Both $\delta^{13}C$ and $\delta^{18}O$ are clearly distinct from the Helvetic marine carbonate signature (gray box in Figure 4a), and $\delta^{13}C$ is much lighter compared to other carbonates interpreted to be derived from meteoric fluids (e.g., Cardello et al., 2024). The highly radiogenic $^{87}Sr/^{86}Sr$ ratios observed across carbonate samples (up to 0.737; Figure 4b, Table S3) indicate that carbonates precipitated from a fluid that interacted variably with the host crystalline basement (e.g., Burkhard et al., 1992; Challandes et al., 2008; Egli et al., 2016; Marquer & Burkhard, 1992). The relative enrichment of HREE (Figures 4c and 4d) can be interpreted as the result of precipitation from (high-temperature) metamorphic fluid dominated by HCO_3^- and CO_3^{2-} complexant, as well as co-precipitation with REE-bearing accessory (metamorphic) phases preferentially partitioning LREE (e.g., allanite/epidote, monazite, and REE-carbonates observed in our samples; Debruyne et al., 2016; Kalliomäki et al., 2019; Uysal et al., 2007). The variability in C, O, and Sr isotopic compositions, as well as trace element abundances, observed in some samples (e.g., MB samples in Figure 4) may reflect the effects of recrystallization, and/or fluid-rock interaction. Further microstructural and geochemical investigations would be required to assess the extent to which these processes may have influenced the observed isotopic and trace-element signatures. A potential Ca^{2+} source is the deforming shear zone network itself, which is subject to metasomatic reactions and mass transfer (e.g., Goncalves et al., 2012; Marquer & Burkhard, 1992). The compilation of fluid inclusion data in Figure 5 shows the occurrence of a significant CO_2 component (generally <50 vol%) in the low-salinity metamorphic fluids leading to the formation of quartz + feldspar + chlorite + calcite tectonic veins from the crystalline massifs of the Central Alps (Figures 5a and 5b; Cesare et al., 2001; Gnos et al., 2021; Heijboer, 2006; Hoefs & Stalder, 1977; Mullis et al., 1994; Sharp, 2005; Tarantola et al., 2007). $\delta^{13}C$ values of carbonate breccias are comparable at a first approximation to the $\delta^{13}C$ of CO_2 in these fluid inclusions from the ECMs (Figure 5c).

Considering the isotopic fractionation effects between calcite, H_2O and CO_2, we estimated the potential $\delta^{13}C$ and $\delta^{18}O$ composition of the parental fluids for the extended range of temperature at which precipitation potentially occurred (250–500°C; Figure 4a). Adopting the fractionation factors of O'Neil et al. (1969); recalculated by Friedman and O'Neil (1977) for H_2O-Calcite pair, the H_2O of the parental fluid should be depleted in $\delta^{18}O$, ranging between +1.2 and +6.7‰ $\delta^{18}O$ for the extended temperature range considered. Interestingly, these values converge at high temperatures toward the results of similar fractionation modelling performed by Badertscher, Abart, et al. (2002; gray box (B) in Figure 4a) to constrain the composition of metamorphic fluids infiltrating the Glarus thrust. Considering the minimum values of $\delta^{13}C$ observed for carbonate veins in Penninic and ECM basement units (~−10‰ $\delta^{13}C$), the $\delta^{13}C$ signature of the parental fluid converges toward ~−7‰ $\delta^{13}C$ for high temperature precipitation (Figure 4a; adopting the fractionation factors of Chacko et al. (1991) for CO_2-Calcite pair).

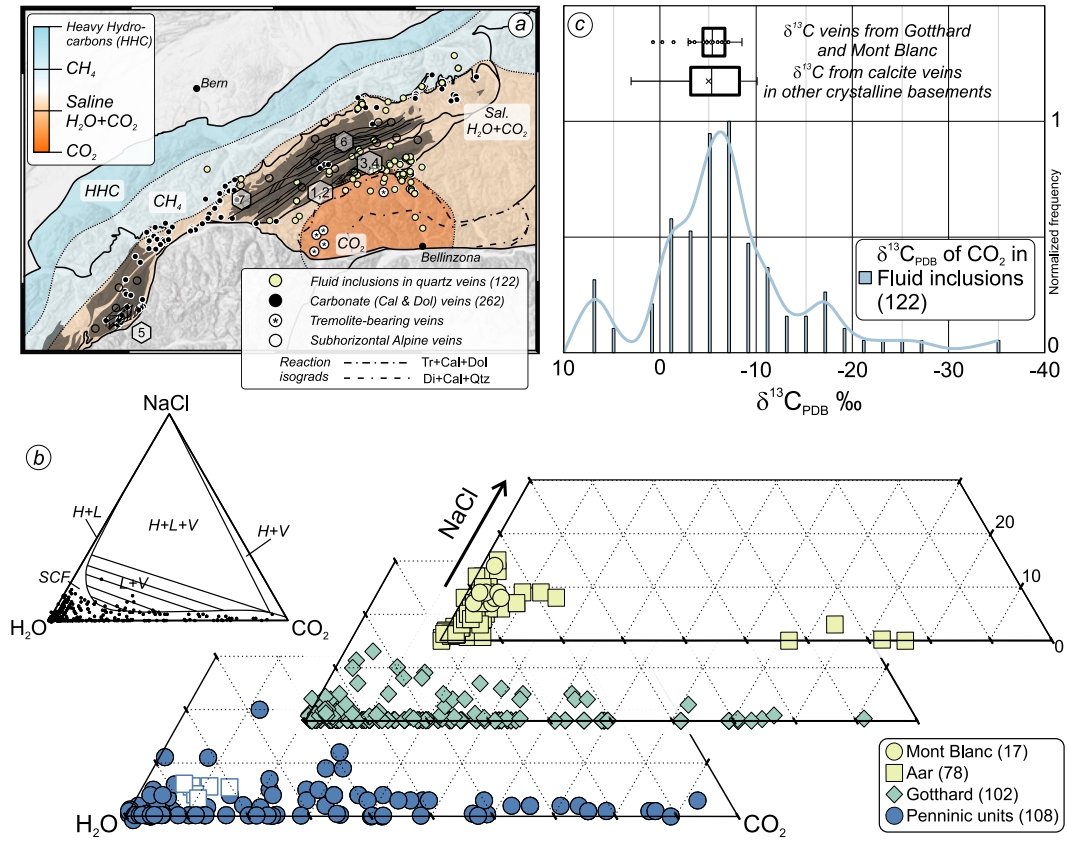


Figure 5. Regional compilation of fluid inclusion composition and isotopic signature. (a) Tectonic sketch of the Western and Central Alps, showing regional domains with distinct fluid inclusion composition and locations of quartz + feldspar + chlorite + calcite veins and of fluid inclusion data included in the compilation (Gnos et al., 2021; Mullis et al., 1994; see references in the main text). Circled asterisks indicate the location of tremolite-bearing veins resulting from infiltration-dehydration reactions in meta-carbonate Penninic units (Meggiolaro et al., 2011; Trommsdorff & Skippen, 1986). Background hillshaded digital terrain model from Nasa SRTM database. (b) H_2O-CO_2-NaCl ternary plot data of fluid inclusion compositions subdivided by location between Penninic units, Gotthard, Aar and Mont Blanc massifs (see main text for references). (c) Normalized frequency histogram representing the $\delta^{13}C$ values of CO_2 from fluid inclusion in tectonic quartz veins of the Central Alps (Cesare et al., 2001; Heijboer, 2006; Hoefs & Stalder, 1977; Mullis et al., 1994; Sharp, 2005; Tarantola et al., 2007), showing also the $\delta^{13}C$ values of carbonates from our data set with the box-and-whisker.

Together, these geochemical signatures are compatible with carbonates precipitated from low-salinity, H_2O-CO_2 metamorphic fluids, which are typically interpreted as resulting from metamorphic devolatilization at the core of the Alpine orogen. These results support the occurrence of a deeply sourced, depleted $\delta^{13}C$ and $\delta^{18}O$ fluid infiltrating the metamorphic basement and Helvetic thrusts in the Central Alps, consistent with the infiltration-related C-O isotopic trends observed in the tectonic veins along Helvetic thrusts (Figure 4a; Badertscher, Abart, et al., 2002; Baumgartner & Valley, 2001; Taylor & Bucher-Nurminen, 1986).

4.2. Transient Fault-Valve Behavior and Metamorphic CO_2 Transfer

Carbonate-bearing breccias document transient CO_2-bearing metamorphic fluid circulation in deformation zones. Carbonate cement is almost exclusively confined to dilatant structures within deformation zones, where it fills newly formed openings, linking mineral precipitation to transient tectonic deformation (Figures 1–3). Similar petrographic associations and genetic environments are inferred for other fault-related ore deposits and mineralization (Robert et al., 1995; Sibson, 1990; Weatherley & Henley, 2013; Williams et al., 2019). Experimental (Brantut, 2020) and theoretical (Weatherley & Henley, 2013) considerations support the common inference that dilation along faults and shear zones induces local and rapid fluctuations in fluid pressure controlling mineral (carbonate) saturation and precipitation, especially at fault jogs (e.g., Figure 1c; Sibson, 1990; Robert et al., 1995). Local rapid dilational events are inferred from injection-like veins and cm-thick fault-veins hosting lattice-bladed

15252027, 2026, 11, Downloaded from https://agupubs.onlinelibrary.wiley.com/doi/10.1029/2026GC013384 by CochraneItalia, Wiley Online Library on [17/11/2026]. See the Terms and Conditions (https://onlinelibrary.wiley.com/terms-and-conditions) on Wiley Online Library for rules of use; OA articles are governed by the applicable Creative Commons License

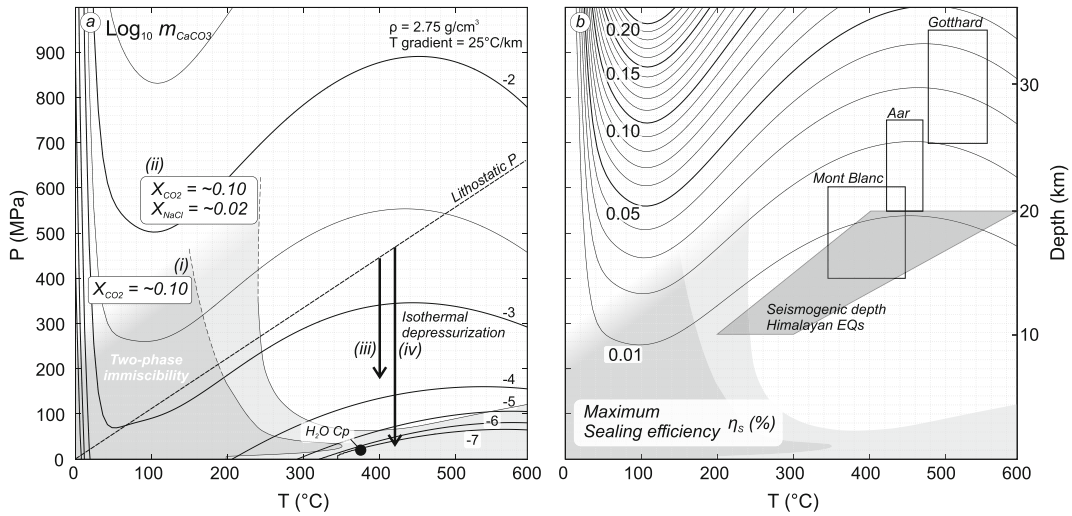


Figure 6. Calcite solubility and sealing efficiency modeling. (a) Pressure-temperature diagram showing the logarithmic contours of calcite molality (m_{CaCO3}, mol/kg) in pure H_2O (Caciagli & Manning, 2003). The diagram also shows the two-phase immiscibility regions (gray areas) for fluids with different compositions from experimental data (Diamond, 2003) and reference therein)): (i) binary H_2O-CO_2 fluid containing 9.9 mol% CO_2 and (ii) ternary H_2O-CO_2-NaCl fluid (representative of more realistic metamorphic fluids composition) containing 9.7 mol% CO_2 and 1.7 mol% NaCl. The bold arrows represent the isothermal depressurization paths from mid-crustal lithostatic fluid pressures: (iii) pressure drop is limited, and the fluid remains a supercritical solution; (iv) pressure drop is large enough to trigger immiscibility and phase separation between a CO_2-rich phase and an aqueous brine. H_2O Cp: critical point conditions for pure H_2O. (b) Pressure-temperature diagram showing the contoured values of the maximum sealing efficiency based on the solubility model shown in (a). The maximum P-T metamorphic conditions for the development and equilibration of shear zones in the *Gotthard*, *Aar*, and *Mont Blanc* are also shown (white hollow boxes) compared to the conditions expected for mid-crustal seismicity (gray prism) in the Himalayan orogen associated with CO_2 emissions.

calcites compatible with seismic slip and fluid boiling (Moncada et al., 2012; Rowe et al., 2012), respectively. At the same time, laminated calcite fault-veins (Figures 2b and 2c) are interpreted to reflect precipitation during repeated fracture-seal cycles (Cox, 2016). Conversely, breccias preserve the evidence of a single brecciation event (i.e., monogenetic breccias, Woodcock et al., 2007). In such breccias, coarse rhombohedral calcite and saddle dolomite cements are rather typical of crystallization in open space during post-deformation stages (Moncada et al., 2012; Woodcock et al., 2007). Furthermore, the combination of reverse shearing on steeply dipping (75° on average) carbonate-bearing shear zones under contractional conditions (Ceccato et al., 2024; Guermani & Pennacchioni, 1998), and the formation of subhorizontal quartz + feldspar + chlorite + calcite extensional veins (Gnos et al., 2021) requires supra-lithostatic fluid pressures potentially in the order of >500 MPa and limited (<25 MPa) differential stress (Text S3, Figure S4 in Supporting Information S1). These features are consistent with transient *fault-valve* behavior (Sibson, 1990) operating at mid-crustal conditions (>350°C–400°C, >500 MPa). The lack of multiple brittle-ductile overprinting suggests that the studied structures record discrete episodes of fracturing and fluid flow, followed by carbonate precipitation and sealing, occurring over timescales much shorter than those required for ductile creep to develop. The structural and geochemical evidence supports a close association between transient deformation, permeability generation, and CO_2 transfer.

4.3. Dilation, Carbonate Precipitation, and Permeability Dynamics

Dilation along faults induces isothermal depressurization, which, in turn, directly affects carbonate solubility in CO_2-bearing fluids (Figure 6a). Calcite precipitation can be described by the simplified equilibrium reaction:

$$Ca^{2+} + CO_{2(aq)} + H_2O \leftrightarrow CaCO_3 + 2H^+$$

where $CO_{2(aq)}$ is the dominant dissolved carbon species in metamorphic fluids (Caciagli & Manning, 2003). Calcite solubility in pure H_2O increases with pressure and reaches a maximum under mid-crustal conditions (Figure 6a) (Caciagli & Manning, 2003). The use of pure H_2O represents a simplification of natural fluid

15252027, 2026, 11, Downloaded from https://agupubs.onlinelibrary.wiley.com/doi/10.1029/2026GC013384 by CochraneItalia, Wiley Online Library on [17/11/2026]. See the Terms and Conditions (https://onlinelibrary.wiley.com/terms-and-conditions) on Wiley Online Library for rules of use; OA articles are governed by the applicable Creative Commons License

15252027, 2026, 11, Downloaded from https://agupubs.onlinelibrary.wiley.com/doi/10.1029/2026GC013384 by CochraneItalia, Wiley Online Library on [17/11/2026]. See the Terms and Conditions (https://onlinelibrary.wiley.com/terms-and-conditions) on Wiley Online Library for rules of use; OA articles are governed by the applicable Creative Commons License

compositions but provides a first-order estimate of solubility behavior under mid-crustal conditions. Depending on temperature and fluid composition, extreme isothermal decompression (down to below unit MPa; Brantut, 2020; Weatherley & Henley, 2013) may also trigger phase immiscibility between a supercritical CO_2-rich phase and aqueous brine (Figure 6a), generating a second episode of dilatancy-driven fluid immiscibility along the ascending flow path of metamorphic fluids (Groppo et al., 2022; Kaszuba et al., 2006). Different from pure H_2O (e.g., Williams, 2019), phase immiscibility and boiling might occur in multicomponent $H_2O + CO_2 + NaCl$ metamorphic fluids also at elevated temperatures (Figure 6a; Diamond, 2003; Heinrich, 2007 and references therein). In our case, lattice-bladed calcites (Figures 3a and 3b) testify for the potential occurrence of phase separation and immiscibility (Moncada et al., 2012; Simmons & Christenson, 1994). The development of an immiscible CO_2-rich phase could further promote calcite precipitation from the metamorphic fluid (e.g., Kaszuba, 2003; Kaszuba et al., 2006).

Carbonate precipitation should promote fault sealing and progressive strength recovery within dilatant segments. Depending on the solubility differential between initial and final fluid pressure, a specific volume of calcite ($V_{Calcite}$) can precipitate from the available fluid volume (V_{Fluid}) and partially seal the dilatant volume ($V_{Dilation}$). Similarly to what was previously proposed for quartz precipitation (Williams, 2019; Williams & Fagereng, 2022), we define the sealing efficiency as

$$\eta_s\ (\%) = V_{Calcite}/V_{Fluid}\ \cdot 100$$

where V_{Fluid} is assumed to completely fill the dilation volume $V_{Dilation}$. For pure H_2O fluids, mass-balance constraints based on calcite solubility models (Caciagli & Manning, 2003) indicate that η_s remains <<0.2%, even considering the maximum attainable values of isothermal depressurization (limited by the lithostatic pressure gradient; Figure 6). These estimates indicate that single episodes of dilation-induced isothermal depressurization alone can account for only a fraction of the observed carbonate volumes. Incipient dilation likely initiates carbonate precipitation and transiently increases local permeability, allowing fluid flow in the remaining dilatant open volume. Either repeated dilation-precipitation cycles (up to 10^3–10^4 events) or, more likely, sustained fluid flow volumes, 10^3–10^4 times the $V_{Dilation}$, are required to account for the large quantity of precipitated carbonates observed (Williams & Fagereng, 2022). Such volumes (10^2–10^3 m^3) are also compatible with the time-integrated fluid fluxes estimated for the basement shear zone networks (2–200 m^3/m^2; Marquer & Burkhard, 1992) and Helvetic thrusts (4,500–9,000 m^3/m^2; Badertscher, Abart, et al., 2002).

Carbonate textures in fault-veins support both near-instantaneous precipitation (e.g., lattice-bladed calcite; Moncada et al., 2012), and repeated fracture-precipitation-seal cycles (e.g., laminated fault veins). Instead, the coarse carbonate cement texture in the breccia matrix points toward a slow post-kinematic growth from a low-supersaturated fluid (Woodcock et al., 2007). This suggests that breccia volumes potentially behaved as long-term fluid reservoirs or long-lasting permeability channels for sustained fluid flux in the shear zone network.

4.4. Localized CO_2-Driven Embrittlement Within a Hydrous Shear-Zone Network

In all ECMs, H_2O-driven metamorphic reactions control the rheology and ductile creep of the shear zone network, punctuated by the local development of subhorizontal and fault-parallel veins (e.g., Figures S2a and S2b in Supporting Information S1; Ceccato et al., 2022, 2024; Goncalves et al., 2012; Oliot et al., 2014). Carbonate-bearing structures occur discontinuously and alternate with carbonate-poor shear zone segments.

Localized carbonate precipitation can be explained by the structural control of transient dilation, which is favored in specific sites of the shear zone network prone to positive volumetric strain (e.g., fault jogs; Sibson, 1990). However, the occurrence of both *localized and large* volumes of carbonates requires a more sophisticated explanation, given that a fluid of suitable composition is required to flow in a specific site of the shear zone network for prolonged time for it to occur. This could potentially reflect spatial (or temporal) heterogeneity in the chemo-physical properties of the fluid (McBride et al., 1995). For example, pulsed devolatilization at depth might lead to temporal and spatial variation in the composition of the advected metamorphic fluid (Groppo et al., 2022; Mullis et al., 1994; Rauchenstein-Martinek et al., 2016). Similarly, spatial CO_2 enrichment may be due to local H_2O-driven metamorphic reactions occurring in the shear zone network, leading to consumption of the H_2O component in the H_2O-CO_2 fluid and to the local accumulation and trapping of a non-reactive, non-wetting CO_2-rich phase.

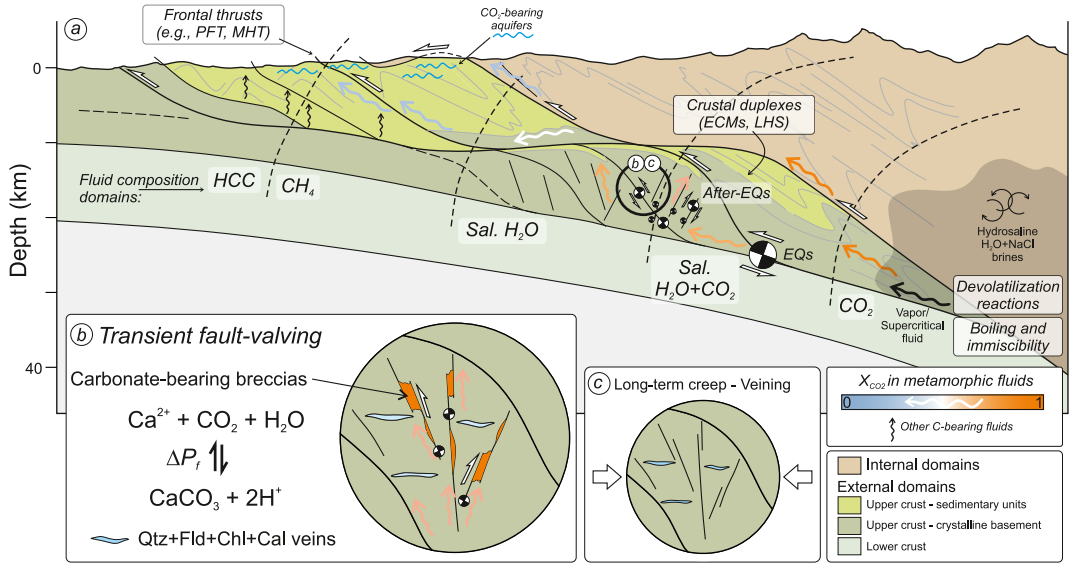


Figure 7. Conceptual model of orogen-scale seismic fluid-flow system. (a) Schematic cross section of a collisional orogen illustrating fluid transfer (orange to light blue undulated arrows) from deep sources to surface sinks (depicted as CO_2-bearing aquifers). Internal domains undergo devolatilization, releasing low-salinity H_2O-CO_2 fluids and hydrosaline brines; the latter are associated with high-conductivity anomalies (shaded area) (Groppo et al., 2022; Lemonnier et al., 1999; Rawat et al., 2014). In the External domains (e.g., ECMs; Lesser Himalaya Series, *LHS*), major thrust and crustal duplexes provide permeable pathways. Seismic events (moment tensors) and subsequent aftershock/swarm sequences trigger transient fluid discharge through these crystalline units. Other sources of C-bearing fluids are also highlighted, coming from the maturation of organic matter related to the involvement of sedimentary units in subduction and collision processes (e.g., Tarantola et al., 2007, 2009). (b) Fault-valve behavior: fluid overpressure drives transient dilation, and pressure drops, inducing carbonate precipitation and sealing of the host structures. (c) Post-sealing evolution involves ductile creep, recovery of fluid pressure and the formation of subhorizontal quartz + feldspar + chlorite + calcite veins (Ceccato et al., 2024; Gnos et al., 2021). Recurring fracture-seal cycles promote the progressive upward advection of metamorphic CO_2 toward the surface.

It follows that, the localized occurrence of large volumes of brittle, carbonate-only-bearing breccias, within non-dilatant, viscously deforming shear zone network dominated by H_2O-rich fluids, indicates that fluid chemical composition can actively influence deformation style (e.g., Onasch et al., 2009). CO_2-bearing fluids are characterized by limited mobility in the pore network, due to the decreased wetting properties (Holness, 1992; Watson & Brenan, 1987), and a larger molar volume (Giuntoli et al., 2024; Labotka et al., 2002)—the combination of which may lead to localized fluid pressure build-up, creep strengthening, and fracture initiation (Brenan & Watson, 1988; Chernak et al., 2009). We propose that CO_2-bearing fluids facilitate brittle fracturing (i.e., brecciation) under pressure–temperature conditions where ductile creep would be expected otherwise (e.g., Ceccato & Pennacchioni, 2025; Chernak et al., 2009), similar to what has been reported for ultramafic rocks (e.g., Rovetta et al., 1987; Sørensen et al., 2019).

4.5. Orogen-Scale Advective Flow and Potential Seismicity

Previous studies have proposed the occurrence of an orogenic-scale plumbing system connecting the deep, devolatilizing source regions for metamorphic fluids to the shallow, potentially seismogenic thrust systems in the external domains of the orogen in the Central Alps (Badertscher, Abart, et al., 2002; Burkhard & Kerrich, 1988; Kirschner et al., 1995, 1999; Marquer & Burkhard, 1992; Rossi & Rolland, 2014) (e.g., Figure 7). The compilation of carbonate regional $\delta^{13}C$–$\delta^{18}O$ and fluid inclusion data (Figures 4 and 5) indeed defines a systematic outward decrease in CO_2 abundance, isotopic fractionation, and progressive fluid-rock interaction from the internal devolatilization domain (Mullis et al., 1994; Rauchenstein-Martinek et al., 2016) toward external thrust systems (Burkhard & Kerrich, 1988; Marquer & Burkhard, 1992; Rossi & Rolland, 2014). Badertscher, Abart, et al. (2002) and Kirschner et al. (1999) explained the carbonate $\delta^{13}C$–$\delta^{18}O$ trends observed in the external Helvetic thrusts as resulting from the interaction between a (low-X_{CO_2}) metamorphic fluid and the host Helvetic marine carbonate units (bold dashed curve in Figure 4a). The $\delta^{13}C$–$\delta^{18}O$ composition of this low-X_{CO_2}

15252027, 2026, 11, Downloaded from https://agupubs.onlinelibrary.wiley.com/doi/10.1029/2026GC013384 by CochraneItalia, Wiley Online Library on [17/11/2026]. See the Terms and Conditions (https://onlinelibrary.wiley.com/terms-and-conditions) on Wiley Online Library for rules of use; OA articles are governed by the applicable Creative Commons License

15252027, 2026, 11, Downloaded from https://agupubs.onlinelibrary.wiley.com/doi/10.1029/2026GC013384 by CochraneItalia, Wiley Online Library on [17/11/2026]. See the Terms and Conditions (https://onlinelibrary.wiley.com/terms-and-conditions) on Wiley Online Library for rules of use; OA articles are governed by the applicable Creative Commons License

metamorphic fluid is very similar to the carbonate vein $\delta^{13}C$–$\delta^{18}O$ observed in the Penninic and External crystalline basements ("Metamorphic fluids" box in Figure 4a; Badertscher, Abart, et al., 2002; Kirschner et al., 1999). Comparable isotopic and fluid composition patterns have been reported from active collisional belts, including the Himalaya (Evans et al., 2008) and the Apennines (Chiodini et al., 2020), where metamorphic-CO_2 emissions at the surface are indirectly inferred to be related to seismic events.

Our $\delta^{13}C$–$\delta^{18}O$ data bolster this interpretation and the orogen-scale advection model (Badertscher, Abart, et al., 2002; Badertscher, Beaudoin, et al., 2002; ; Burkhard & Kerrich, 1988; Marquer & Burkhard, 1992; Rossi & Rolland, 2014) provides evidence for mid-crustal fluid flow and carbonate precipitation. In this framework, the Alpine shear zone networks represent the middle-crustal segment of this orogenic plumbing system, acting as an intermittently permeable barrier to the upward advection of pressurized CO_2-bearing fluids (Figure 7). As commonly inferred from fault-valve vein systems, the development of carbonate-bearing structures might be accompanied by swarm-type seismicity driven by supra-lithostatic fluid pressures (e.g., Cox, 2016; Micklethwaite & Cox, 2006; Robert et al., 1995; Sibson, 1990). These structures developed at mid-crustal conditions (300°C–400°C and 0.5–0.8 GPa) comparable to the structural levels at which fluid-driven aftershocks and seismic swarms are recorded collisional belts, along similarly oriented structures within crystalline units (Figure 7; e.g., Adhikari et al., 2021; Mendoza et al., 2019). Indeed, fault-valving driven by carbon-bearing fluids is consistent with models of fluid overpressure and transient, seismic deformation invoked for active orogens where CO_2 remobilization is temporally and spatially linked to aftershock seismicity (Collettini et al., 2008; Girault et al., 2018; Groppo et al., 2022; Miller et al., 2004). The sealing efficiency along such seismogenic structures may be <0.05% under peak P-T conditions of shear zone deformation in active collisional belts (Lemonnier et al., 1999; Rawat et al., 2014; Figure 6b), suggesting the occurrence of transiently permeable pathways at mid-crustal conditions beneath currently deforming orogens. Adopting the advective system of the Central Alps as fossil analogue, the metamorphic fluids responsible for such mid-crustal aftershock and swarm-type seismicity are multicomponent, $H_2O + CO_2 + NaCl$ fluids, with a rather diluted CO_2 content (<50 vol%).

4.6. Implications for Carbon Cycling

The Alpine case study indicates that mid-crustal deformation regulates the timing and style of metamorphic CO_2 transfer rather than its total magnitude. This process operates episodically in shear zones throughout much of the collisional orogen history (Oligocene-Miocene time in the Alps; Ceccato et al., 2024; Egli et al., 2016; Rolland et al., 2008; Rossi & Rolland, 2014). Carbonate-bearing breccias and veins record localized and shorter-lived flow and precipitation events associated with transient permeability enhancement in limited crustal volumes. Order-of-magnitude estimates indicate that the carbonate volume preserved within one cubic kilometer of the crystalline massif corresponds to $\sim 3 \cdot 10^4$ m^3 of calcite (~18 kt of CO_2; $4.1 \cdot 10^8$ mol of CO_2; Text S4 in Supporting Information S1). Extrapolating these estimates to the exposed area of the ECMs (~500 km^2 for Mont Blanc; larger than 2000 km^2 for Aar-Gotthard), we obtain carbon storage values of the order of 9 Mt/km of CO_2 ($1.17 \cdot 10^{11}$ mol/km of CO_2) in the Mont Blanc, and 36 Mt/km of CO_2 ($4.68 \cdot 10^{11}$ mol/km of CO_2) in the Aar-Gotthard. Extrapolation of these values to the entire (European) Alpine orogen (~200,000 km^2) leads to an estimation of about $\sim 5 \cdot 10^{13}$ mol of CO_2 per km depth of the orogen mid crust. Our estimates refer to the results of a CO_2-capture process that lasted for several million years during Alpine orogenesis, although potentially occurring transiently over shorter time periods. The estimated (area-integrated) CO_2 fluxes for actively degassing orogens vary between $1.1 \cdot 10^{10}$ and $>2 \cdot 10^{12}$ mol/yr (Becker et al., 2008; Chiodini et al., 2020; Evans et al., 2008; Groppo et al., 2017; Kerrick & Caldeira, 1998; Liu et al., 2025; Pradhan & Sen, 2024). Given the uncertainty on the duration, regional extent, and potential episodicity of the CO_2-fixation process, we cannot provide a reliable comparison between observed flux estimates and our calculations. Most likely, the process described here would affect in a very limited way the yearly CO_2 orogenic flux, potentially storing limited fractions (<0.01–0.001) of the overall orogenic CO_2 flow, thus indicating that quartz-rich mid-crust has limited capacity as a long-term carbon reservoir at the orogen scale. The significance of these structures lies not in the magnitude of carbon stored, but in revealing how carbon is transferred through the crust. By imposing episodic permeability spikes under near-lithostatic fluid pressures, mid-crustal shear zones regulate the temporal transfer of metamorphic CO_2, indicating that crustal carbon flux is regulated by (potentially seismic) dynamic processes (Figure 7). Mid-crustal deformation influences when and where CO_2 is released, without substantially increasing net crustal carbon retention during orogenesis.

15252027, 2026, 11, Downloaded from https://agupubs.onlinelibrary.wiley.com/doi/10.1029/2026GC013384 by CochraneItalia, Wiley Online Library on [17/11/2026]. See the Terms and Conditions (https://onlinelibrary.wiley.com/terms-and-conditions) on Wiley Online Library for rules of use; OA articles are governed by the applicable Creative Commons License

5. Conclusions

In collisional orogens, carbonate-bearing breccias represent a fossil analog of coupled transient (potentially seismic) deformation, permeability development, and CO_2-bearing metamorphic fluid flow at mid-crustal conditions. In the regions where breccias are reported, metamorphic fluids are CO_2-bearing but rather diluted (CO_2 < 50 vol%). Potentially seismic fault-valving regulates dynamic and transient permeability pulses, induced by supra-lithostatic CO_2-bearing fluids. Due to their chemo-physical properties, CO_2-bearing fluids may have promoted localized brittle failure in a shear zone network deforming otherwise by viscous flow assisted by H_2O-driven metamorphic reactions. Brittle deformation induces dilatancy, causing carbonate precipitation, which is incapable of efficiently re-sealing and healing the dilatant volume, therefore promoting longer-term permeability and upward advection of CO_2-bearing metamorphic fluids. Deformation-induced carbonate precipitation might be a potentially relevant sink in the global orogenic carbon cycle only if carbonate precipitation and brittle deformation occur over shorter time scales typical of fluid-driven seismic cycle (10^3–10^5 years; Cox, 2016).

This case study provides a geological analogue for how transient permeability and (potentially seismogenic) fault-valving may contribute to episodic CO_2 transfer in the middle crust. Carbonate-bearing breccias may represent the fossil analogue of fluid-(CO_2)-driven aftershocks and swarm-type activity, which is currently observed in active collisional belts associated with surficial CO_2 emissions. Our observations suggest that similar mechanisms may operate in other tectonic settings hosting CO_2-rich fluids—including continental rifting (Lee et al., 2016; Wang et al., 2026), and post-orogenic extension (Liu et al., 2024; Miller et al., 2004; Tamburello et al., 2018). By linking transient crustal permeability to seismic processes, our findings confirm that the timing and localization of CO_2 emissions are dynamically regulated by deformation.

Conflict of Interest

The authors declare no conflicts of interest relevant to this study.

Acknowledgments
This work has received funding from the European Union's Horizon Europe research and innovation programme under Marie Sklodowska-Curie, Grant 101205582—Project "SEISMI-COS: Seismogenic behavior of continental subduction: insights from rheology and petrophysics." Part of the work was performed with the support of Project MIUR—Dipartimenti di Eccellenza TECLA, Department of Earth and Environmental Sciences, University of Milano-Bicocca. This work has also been funded within the framework of the Regional Programme of the European Regional Development Fund 2021–2027 of Regione Lombardia (PR FESR 2021-2027, Action 1.1.3, in compliance with European Regulation No. 1060/2021), following the public call "Collabora&Innova." Project "CO_2: from a global problem to a tool to implement circularity—CO-Tool" (Project ID 6144755). The authors thank Luiz G. F. Morales of ScopeM (Scientific Center of Optical and Electron Microscopy at ETH) for their support and assistance in this work. Madalina Jaggi is acknowledged for support and implementation of stable isotope analyses. Remy Lüchinger is warmly thanked for the support in sample and thin section preparation. We are grateful to Neil Mancktelow and Alberto Vitale Brovarone for their fruitful insights and discussions. Fieldwork benefited from the logistical support of the SAC-CAS Capanna Piansecco.

Availability Statement

Results of geochemical and isotopic analyses of carbonates, as well as Matlab scripts adopted for computing Figure 6 diagrams, are reported as Tables S1–S3, and available for download from http://hdl.handle.net/20.500.11850/798154 (Ceccato, 2026).

References

Adhikari, L. B., Bollinger, L., Vergne, J., Lambotte, S., Chanard, K., Laporte, M., et al. (2021). Orogenic collapse and stress adjustments revealed by an intense seismic swarm following the 2015 Gorkha earthquake in Nepal. *Frontiers in Earth Science*, *9*, 659937. https://doi.org/10.3389/feart.2021.659937

Badertscher, N. P., Abart, R., Burkhard, M., & McCaig, A. (2002). Fluid flow pathways along the Glarus overthrust derived from stable and Sr-isotope patterns. *American Journal of Science*, *302*, 517–547. https://doi.org/10.2475/ajs.302.6.517

Badertscher, N. P., Beaudoin, G., Therrien, R., & Burkhard, M. (2002). Glarus overthrust: A major pathway for the escape of fluids out of the Alpine orogen. *Geology*, *30*(10), 875–878. https://doi.org/10.1130/0091-7613(2002)030<0875:goampf>2.0.co;2

Badertscher, N. P., & Burkhard, M. (2002). Brittle–ductile deformation in the Glarus thrust Lochseiten (LK) calc-mylonite. *Terra Nova*, *12*(6), 281–288. https://doi.org/10.1046/j.1365-3121.2000.00310.x

Baumgartner, L. P., & Valley, J. W. (2001). Stable isotope transport and contact metamorphic fluid flow. *Reviews in Mineralogy and Geochemistry*, *43*(1), 415–467. https://doi.org/10.2138/gsrmg.43.1.415

Becker, J. A., Bickle, M. J., Galy, A., & Holland, T. J. (2008). Himalayan metamorphic CO_2 fluxes: Quantitative constraints from hydrothermal springs. *Earth and Planetary Science Letters*, *265*(3–4), 616–629. https://doi.org/10.1016/j.epsl.2007.10.046

Brantut, N. (2020). Dilatancy-induced fluid pressure drop during dynamic rupture: Direct experimental evidence and consequences for earthquake dynamics. *Earth and Planetary Science Letters*, *538*, 116179. https://doi.org/10.1016/j.epsl.2020.116179

Breitenbach, S. F. M., & Bernasconi, S. M. (2011). Carbon and oxygen isotope analysis of small carbonate samples (20 to 100 µg) with a GasBench II preparation device. *Rapid Communications in Mass Spectrometry*, *25*(13), 1910–1914. https://doi.org/10.1002/rcm.5052

Brenan, J., & Watson, B. E. (1988). Fluids in the lithosphere, 2. Experimental constraints on CO_2 transport in dunite and quartzite at elevated P-T conditions with implications for mantle and crustal decarbonation processes. *Earth and Planetary Science Letters*, *91*(1–2), 141–158. https://doi.org/10.1016/0012-821X(88)90157-4

Burkhard, M., & Kerrich, R. (1988). Fluid regimes in the deformation of the Helvetic nappes, Switzerland, as inferred from stable isotope data. *Contributions to Mineralogy and Petrology*, *99*(4), 416–429. https://doi.org/10.1007/BF00371934

Burkhard, M., Kerrich, R., Maas, R., & Fyfe, W. S. (1992). Stable and Sr-isotope evidence for fluid advection during thrusting of the Glarus Nappe (Swiss Alps). *Contributions to Mineralogy and Petrology*, *112*(2–3), 293–311. https://doi.org/10.1007/BF00310462

Caciagli, N. C., & Manning, C. E. (2003). The solubility of calcite in water at 6–16 kbar and 500–800°C. *Contributions to Mineralogy and Petrology*, *146*(3), 275–285. https://doi.org/10.1007/s00410-003-0501-y

Cardello, G. L., Bernasconi, S. M., Fellin, M. G., Rahn, M., Rosskopf, R., Maden, C., & Mancktelow, N. S. (2024). Carbonate deformation through the brittle-ductile transition: The case of the SW Helvetic nappes, Switzerland. *Journal of Structural Geology*, *181*, 105083. https://doi.org/10.1016/j.jsg.2024.105083

Ceccato, A. (2026). Carbonate chemical analyses and scripts [Dataset]. *ETH Research Collection*. https://doi.org/10.3929/ethz-c-000798154

Ceccato, A., Behr, W. M., Zappone, A. S., Tavazzani, L., & Giuliani, A. (2024). Structural evolution, exhumation rates, and rheology of the European crust during alpine collision: Constraints from the rotondo Granite—Gotthard Nappe. *Tectonics*, *43*(6), e2023TC008219. https://doi.org/10.1029/2023TC008219

Ceccato, A., Goncalves, P., & Menegon, L. (2022). On the petrology and microstructures of small-scale ductile shear zones in granitoid rocks: An overview. *Journal of Structural Geology*, *161*, 104667. https://doi.org/10.1016/j.jsg.2022.104667

Ceccato, A., & Pennacchioni, G. (2025). Fluid-mediated transition from dynamic rupturing to aseismic slip at the base of the seismogenic continental crust. *Earth and Planetary Science Letters*, *650*, 119117. https://doi.org/10.1016/j.epsl.2024.119117

Cesare, B., Poletti, E., Boiron, M. C., & Cathelineau, M. (2001). Alpine metamorphism and veining in the Zentralgneis Complex of the SW Tauern Window: A model of fluid–rock interactions based on fluid inclusions. *Tectonophysics*, *336*(1–4), 121–136. https://doi.org/10.1016/S0040-1951(01)00097-X

Chacko, T., Mayeda, T. K., Clayton, R. N., & Goldsmith, J. R. (1991). Oxygen and carbon isotope fractionations between CO_2 and calcite. *Geochimica et Cosmochimica Acta*, *55*(10), 2867–2882. https://doi.org/10.1016/0016-7037(91)90452-B

Challandes, N., Marquer, D., & Villa, I. M. (2008). P-T-t modelling, fluid circulation, and ^{39}Ar-^{40}Ar and Rb-Sr mica ages in the Aar Massif shear zones (Swiss Alps). *Swiss Journal of Geosciences*, *101*(2), 269–288. https://doi.org/10.1007/s00015-008-1260-6

Chernak, L. J., Hirth, G., Selverstone, J., & Tullis, J. (2009). Effect of aqueous and carbonic fluids on the dislocation creep strength of quartz. *Journal of Geophysical Research*, *114*(B4). https://doi.org/10.1029/2008JB005884

Chiodini, G., Cardellini, C., Di Luccio, F., Selva, J., Frondini, F., Caliro, S., et al. (2020). Correlation between tectonic CO_2 Earth degassing and seismicity is revealed by a 10-year record in the Apennines, Italy. *Science Advances*, *6*(35). https://doi.org/10.1126/SCIADV.ABC2938/SUPPL_FILE/ABC2938_SM.PDF

Collettini, C., Cardellini, C., Chiodini, G., De Paola, N., Holdsworth, R. E., & Smith, S. A. F. (2008). Fault weakening due to CO_2 degassing in the Northern Apennines: Short-and long-term processes. *Geological Society, London, Special Publications*, *299*(1), 175–194. https://doi.org/10.1144/SP299.11

Cox, S. F. (2016). Injection-driven swarm seismicity and permeability enhancement: Implications for the dynamics of hydrothermal ore systems in high Fluid-Flux, overpressured faulting Regimes—An invited paper. *Economic Geology*, *111*(3), 559–587. https://doi.org/10.2113/econgeo.111.3.559

Debruyne, D., Hulsbosch, N., & Muchez, P. (2016). Unraveling rare earth element signatures in hydrothermal carbonate minerals using a source–sink system. *Ore Geology Reviews*, *72*, 232–252. https://doi.org/10.1016/j.oregeorev.2015.07.022

Diamond, L. W. (2003). Introduction to gas-bearing, aqueous fluid inclusions. In I. Samson, A. Anderson, & D. Marshall (Eds.), *Fluid inclusions: Analysis and interpretation* (Vol. 32, pp. 101–158). Mineralogical Association of Canada. https://doi.org/10.3749/9780921294672.ch05

Dietrich, D., McKenzie, J. A., & Song, H. (1983). Origin of calcite in syntectonic veins as determined from carbon-isotope ratios. *Geology*, *11*(9), 547–551. https://doi.org/10.1130/0091-7613(1983)11<547:oocisv>2.0.co;2

Egli, D., Müller, W., & Mancktelow, N. (2016). Laser-cut Rb–Sr microsampling dating of deformational events in the Mont Blanc-Aiguilles Rouges region (European Alps). *Terra Nova*, *28*(1), 35–42. https://doi.org/10.1111/ter.12184

Evans, M. J., Derry, L. A., France-Lanord, C., Evans, M. J., Derry, L. A., & France, C. (2008). Degassing of metamorphic carbon dioxide from the Nepal Himalaya. *Geochemistry, Geophysics, Geosystems*, *9*(4), 4021. https://doi.org/10.1029/2007GC001796

Ferrill, D. A., Morris, A. P., Evans, M. A., Burkhard, M., Groshong, R. H., & Onasch, C. M. (2004). Calcite twin morphology: A low-temperature deformation geothermometer. *Journal of Structural Geology*, *26*(8), 1521–1529. https://doi.org/10.1016/j.jsg.2003.11.028

Fitzpayne, A., Giuliani, A., Howarth, G. H., Peters, B. J., Fehr, M. A., & Maas, R. (2023). Major-trace-element and Sr-Nd-Hf isotope geochemistry of diamondiferous dykes from Tonguma and Koidu, Sierra Leone: Highly micaceous kimberlites formed by assimilation of metasomatised lithospheric mantle rocks. *Chemical Geology*, *630*, 121475. https://doi.org/10.1016/j.chemgeo.2023.121475

Frezzotti, M. L., Peccerillo, A., & Panza, G. (2009). Carbonate metasomatism and CO_2 lithosphere–asthenosphere degassing beneath the Western Mediterranean: An integrated model arising from petrological and geophysical data. *Chemical Geology*, *262*(1–2), 108–120. https://doi.org/10.1016/J.CHEMGEO.2009.02.015

Friedman, I., & O'Neil, J. R. (1977). Compilation of stable isotope fractionation factors of geochemical interest (No. 440-KK).

Fusseis, F., Regenauer-Lieb, K., Liu, J., Hough, R. M., & De Carlo, F. (2009). Creep cavitation can establish a dynamic granular fluid pump in ductile shear zones. *Nature*, *459*(7249), 974–977. https://doi.org/10.1038/nature08051

Girault, F., Adhikari, L. B., France-Lanord, C., Agrinier, P., Koirala, B. P., Bhattarai, M., et al. (2018). Persistent CO_2 emissions and hydrothermal unrest following the 2015 earthquake in Nepal. *Nature Communications*, *9*(1), 1–10. https://doi.org/10.1038/s41467-018-05138-z

Giuntoli, F., Menegon, L., Siron, G., Cognigni, F., Leroux, H., Compagnoni, R., et al. (2024). Methane-hydrogen-rich fluid migration may trigger seismic failure in subduction zones at forearc depths. *Nature Communications*, *15*(1), 1–16. https://doi.org/10.1038/s41467-023-44641-w

Gnos, E., Mullis, J., Ricchi, E., Bergemann, C., Janots, E., & Berger, A. (2021). Episodes of fissure formation in the Alps: Connecting quartz fluid inclusion, fissure monazite age, and fissure orientation data. *Swiss Journal of Geosciences*, *114*(1), 1–25. https://doi.org/10.1186/S00015-021-00391-9

Goncalves, P., Oliot, E., Marquer, D., & Connolly, J. A. D. (2012). Role of chemical processes on shear zone formation: An example from the Grimsel metagranodiorite (Aar massif, Central Alps). *Journal of Metamorphic Geology*, *30*(7), 703–722. https://doi.org/10.1111/j.1525-1314.2012.00991.x

Groppo, C., Rolfo, F., Castelli, D., & Mosca, P. (2017). Metamorphic CO_2 production in collisional orogens: Petrological constraints from phase diagram modeling of Himalayan, scapolite-bearing, calc-silicate rocks in the NKC (F) MAS (T)-HC system. *Journal of Petrology*, *58*(1), 53–83. https://doi.org/10.1093/petrology/egx005

Groppo, C., Rolfo, F., & Frezzotti, M. L. (2022). CO2 outgassing during collisional orogeny is facilitated by the generation of immiscible fluids. *Communications Earth & Environment*, *3*(1), 1–11. https://doi.org/10.1038/s43247-022-00340-w

Guermani, A., & Pennacchioni, G. (1998). Brittle precursors of plastic deformation in a granite: An example from the Mont Blanc massif (Helvetic, western Alps). *Journal of Structural Geology*, *20*(2–3), 135–148. https://doi.org/10.1016/S0191-8141(97)00080-1

Guillong, M., Hametner, K., Reusser, E., Wilson, S. A., & Günther, D. (2005). Preliminary Characterisation of New Glass Reference Materials (GSA-1G, GSC-1G, GSD-1G and GSE-1G) by Laser Ablation-Inductively Coupled Plasma-Mass Spectrometry using 193 nm, 213 nm and 266 nm wavelengths. *Geostandards and Geoanalytical Research*, *29*(3), 315–331. https://doi.org/10.1111/j.1751-908X.2005.tb00903.x

Heijboer, T. C. (2006). Origin and pathways of pro- and retro-grade fluids, PTt paths and fluid-mineral equilibria from Alpine veins of the Central Alps: Case studies of the Fibbia and Amsteg areas PhD-Thesis, (September).

15252027, 2026, 11, Downloaded from https://agupubs.onlinelibrary.wiley.com/doi/10.1029/2026GC013384 by CochraneItalia, Wiley Online Library on [17/11/2026]. See the Terms and Conditions (https://onlinelibrary.wiley.com/terms-and-conditions) on Wiley Online Library for rules of use; OA articles are governed by the applicable Creative Commons License

Heinrich, W. (2007). Fluid immiscibility in metamorphic rocks. *Reviews in Mineralogy and Geochemistry*, *65*(1), 389–430. https://doi.org/10.2138/rmg.2007.65.12

Hoefs, J., & Stalder, H. A. (1977). Die C-Isotopenzusammensetzung von CO_2-haltigen Flüssigkeitseinschlüssen in Kluftquarzen der Zentralalpen. https://doi.org/10.5169/SEALS-44439

Holness, M. B. (1992). Equilibrium dihedral angles in the system quartz-CO2H2ONaCl at 800°C and 1–15 kbar: The effects of pressure and fluid composition on the permeability of quartzites. *Earth and Planetary Science Letters*, *114*(1), 171–184. https://doi.org/10.1016/0012-821X(92)90159-S

Irrgeher, J., Galler, P., & Prohaska, T. (2016). 87 Sr/86 Sr isotope ratio measurements by laser ablation multicollector inductively coupled plasma mass spectrometry: Reconsidering matrix interferences in bioapatites and biogenic carbonates. *Spectrochimica Acta Part B: Atomic Spectroscopy*, *125*, 31–42. https://doi.org/10.1016/j.sab.2016.09.008

Irwin, W. P., & Barnes, I. (1980). Tectonic relations of carbon dioxide discharges and earthquakes. *Journal of Geophysical Research*, *85*(B6), 3115–3121. https://doi.org/10.1029/JB085IB06P03115

Jochum, K. P., Weis, U., Stoll, B., Kuzmin, D., Yang, Q., Raczek, I., et al. (2011). Determination of reference values for NIST SRM 610–617 Glasses Following ISO Guidelines. *Geostandards and Geoanalytical Research*, *35*(4), 397–429. https://doi.org/10.1111/j.1751-908X.2011.00120.x

Kalliomäki, H., Wagner, T., Fusswinkel, T., & Schultze, D. (2019). Textural evolution and trace element chemistry of hydrothermal calcites from Archean gold deposits in the Hattu schist belt, eastern Finland: Indicators of the ore-forming environment. *Ore Geology Reviews*, *112*, 103006. https://doi.org/10.1016/j.oregeorev.2019.103006

Kaszuba, J. P., Janecky, D. R., & Snow, M. G. (2003). Carbon dioxide reaction processes in a model brine aquifer at 200°C and 200 bars: Implications for geologic sequestration of carbon. *Applied Geochemistry*, *18*(7), 1065–1080. https://doi.org/10.1016/S0883-2927(02)00239-1

Kaszuba, J. P., Williams, L. L., Janecky, D. R., Hollis, W. K., Kaszuba, J. P., Williams, L. L., et al. (2006). Immiscible CO_2-H_2O fluids in the shallow crust. *Geochemistry, Geophysics, Geosystems*, *7*(10), 10003. https://doi.org/10.1029/2005GC001107

Kerrick, D. M., & Caldeira, K. (1998). Metamorphic CO_2 degassing from orogenic belts. *Chemical Geology*, *145*(3–4), 213–232. https://doi.org/10.1016/S0009-2541(97)00144-7

Kirschner, D. L., Masson, H., & Sharp, Z. D. (1999). Fluid migration through thrust faults in the Helvetic nappes (Western Swiss Alps). *Contributions to Mineralogy and Petrology*, *136*(1–2), 169–183. https://doi.org/10.1007/s004100050530

Kirschner, D. L., Sharp, Z. D., & Masson, H. (1995). Oxygen isotope thermometry of quartz-calcite veins: Unraveling the thermal-tectonic history of the subgreenschist facies Morcles nappe (Swiss Alps). *GSA Bulletin*, *107*(10), 1145–1156. https://doi.org/10.1130/0016-7606(1995)107<1145:oitoqc>2.3.co;2

Labotka, T. C., Anovitz, L. M., & Blencoe, J. G. (2002). Pore pressure during metamorphism of carbonate rock: Effect of volumetric properties of H_2O–CO_2 mixtures. *Contributions to Mineralogy and Petrology*, *144*(3), 305–313. https://doi.org/10.1007/s00410-002-0398-x

Lee, H., Muirhead, J. D., Fischer, T. P., Ebinger, C. J., Kattenhorn, S. A., Sharp, Z. D., & Kianji, G. (2016). Massive and prolonged deep carbon emissions associated with continental rifting. *Nature Geoscience*, *9*(2), 145–149. https://doi.org/10.1038/ngeo2622

Lemonnier, C., Marquis, G., Perrier, F., Avouac, J. P., Chitrakar, G., Kafle, B., et al. (1999). Electrical structure of the Himalaya of central Nepal: High conductivity around the mid-crustal ramp along the MHT. *Geophysical Research Letters*, *26*(21), 3261–3264. https://doi.org/10.1029/1999GL008363

Liu, W., Zhang, M., Liu, Y., Cui, L., Sano, Y., Zhou, X., et al. (2024). Massive crustal carbon mobilization and emission driven by India underthrusting Asia. *Communications Earth & Environment*, *5*(1), 271. https://doi.org/10.1038/s43247-024-01438-z

Liu, Y., Liu, W., Xie, X. G., Liu, C. Q., Zhang, M., Sano, Y., et al. (2025). Extensional rifts liberate substantial amounts of deeply-sourced CO_2 from the Himalayan-Tibetan orogen. *Science Bulletin*, *71*(3), 530–533. https://doi.org/10.1016/j.scib.2025.09.055

Looser, N., Aschwanden, L., Wohlwend, S., Guillong, M., Rickli, J., Schneeberger, R., & Bernasconi, S. M. (2025). Constraining 200 million years of geodynamic evolution of the North Alpine foreland at million-year resolution using clumped isotopes and U-Pb dating of diagenetic carbonates. *Earth and Planetary Science Letters*, *667*, 119410. https://doi.org/10.1016/j.epsl.2025.119410

Luisier, C., Baumgartner, L. P., Putlitz, B., & Vennemann, T. (2021). Whiteschist genesis through metasomatism and metamorphism in the Monte Rosa nappe (Western Alps). *Contributions to Mineralogy and Petrology*, *176*(1), 10. https://doi.org/10.1007/s00410-020-01759-0

Malusà, M. G., Brandmayr, E., Panza, G. F., Romanelli, F., Ferrando, S., & Frezzotti, M. L. (2022). An explosive component in a December 2020 Milan earthquake suggests outgassing of deeply recycled carbon. *Communications Earth & Environment*, *3*(1), 1–6. https://doi.org/10.1038/s43247-021-00336-y

Marquer, D., & Burkhard, M. (1992). Fluid circulation, progressive deformation and mass-transfer processes in the upper crust: The example of basement-cover relationships in the External Crystalline Massifs, Switzerland. *Journal of Structural Geology*, *14*(8–9), 1047–1057. https://doi.org/10.1016/0191-8141(92)90035-U

Marquer, D., Petrucci, E., & Iacumin, P. (1994). Fluid advection in shear zones: Evidence from geological and geochemical relationships. In *The aiguilles rouges massif (Western alps, Switzerland)*. https://doi.org/10.5169/SEALS-56337

McBride, E. F., Milliken, K. L., Cavazza, W., Cibin, U., Fontana, D., Picard, M. D., & Zuffa, G. G. (1995). Heterogeneous distribution of calcite cement at the outcrop Scale in tertiary sandstones, Northern Apennines, Italy. *AAPG Bulletin*, *79*(7), 1044–1062. https://doi.org/10.1306/8D2B21C3-171E-11D7-8645000102C1865D

Meggiolaro, V., Sapigni, M., & Fioretti, A. M. (2011). Tremolite–calcite veins in the footwall of the Simplon Fault, Antigorio Valley, Lepontine Alps (Italy). *Swiss Journal of Geosciences*, *104*(3), 355–365. https://doi.org/10.1007/s00015-011-0074-0

Mendoza, M. M., Ghosh, A., Karplus, M. S., Klemperer, S. L., Sapkota, S. N., Adhikari, L. B., & Velasco, A. (2019). Duplex in the Main Himalayan Thrust illuminated by aftershocks of the 2015 Mw 7.8 Gorkha earthquake. *Nature Geoscience*, *12*(12), 1018–1022. https://doi.org/10.1038/s41561-019-0474-8

Mercolli, I., Skippen, G., & Trommsdorff, V. (1987). The tremolite veins of Campolungo and their genesis. *Schweizerische Mineralogische und Petrographische Mitteilungen*, *67*(1–2), 75–84. https://doi.org/10.5169/seals-51588

Micklethwaite, S., & Cox, S. F. (2006). Progressive fault triggering and fluid flow in aftershock domains: Examples from mineralized Archaean fault systems. *Earth and Planetary Science Letters*, *250*(1–2), 318–330. https://doi.org/10.1016/j.epsl.2006.07.050

Miller, S. A., Collettini, C., Chiaraluce, L., Cocco, M., Barchi, M., & Kaus, B. J. P. (2004). Aftershocks driven by a high-pressure CO_2 source at depth. *Nature*, *427*(6976), 724–727. https://doi.org/10.1038/nature02251

Moncada, D., Mutchler, S., Nieto, A., Reynolds, T. J., Rimstidt, J. D., & Bodnar, R. J. (2012). Mineral textures and fluid inclusion petrography of the epithermal Ag–Au deposits at Guanajuato, Mexico: Application to exploration. *Journal of Geochemical Exploration*, *114*, 20–35. https://doi.org/10.1016/j.gexplo.2011.12.001

15252027, 2026, 11, Downloaded from https://agupubs.onlinelibrary.wiley.com/doi/10.1029/2026GC013384 by CochraneItalia, Wiley Online Library on [17/11/2026]. See the Terms and Conditions (https://onlinelibrary.wiley.com/terms-and-conditions) on Wiley Online Library for rules of use; OA articles are governed by the applicable Creative Commons License

Mulder, J., Hagen-Peter, G., Ubide, T., Andreasen, R., Kooijman, E., Kielman-Schmitt, M., et al. (2023). New reference materials, analytical procedures and data reduction strategies for Sr isotope measurements in geological materials by LA-MC-ICP-MS. *Geostandards and Geoanalytical Research*, *47*(2), 311–336. https://doi.org/10.1111/ggr.12480

Mullis, J., Dubessy, J., Poty, B., & O'Neil, J. (1994). Fluid regimes during late stages of a continental collision: Physical, chemical, and stable isotope measurements of fluid inclusions in fissure quartz from a geotraverse through the Central Alps, Switzerland. *Geochimica et Cosmochimica Acta*, *58*(10), 2239–2267. https://doi.org/10.1016/0016-7037(94)90008-6

Nuriel, P., Weinberger, R., Kylander-Clark, A. R. C., Hacker, B. R., & Craddock, J. P. (2017). The onset of the Dead Sea transform based on calcite age-strain analyses. *Geology*, *45*(7), 587–590. https://doi.org/10.1130/G38903.1

Oliot, E., Goncalves, P., Schulmann, K., Marquer, D., & Lexa, O. (2014). Mid-crustal shear zone formation in granitic rocks: Constraints from quantitative textural and crystallographic preferred orientations analyses. *Tectonophysics*, *612*, 63–80. https://doi.org/10.1016/j.tecto.2013.11.032

Onasch, C. M., Dunne, W. M., Cook, J. E., & O'Kane, A. (2009). The effect of fluid composition on the behavior of well cemented, quartz-rich sandstone during faulting. *Journal of Structural Geology*, *31*(9), 960–971. https://doi.org/10.1016/j.jsg.2008.10.010

O'Neil, J. R., Clayton, R. N., & Mayeda, T. K. (1969). Oxygen isotope fractionation in divalent metal carbonates. *The Journal of Chemical Physics*, *51*(12), 5547–5558. https://doi.org/10.1063/1.1671982

Paton, C., Hellstrom, J., Paul, B., Woodhead, J., & Hergt, J. (2011). Iolite: Freeware for the visualisation and processing of mass spectrometric data. *Journal of Analytical Atomic Spectrometry*, *26*(12), 2508–2518. https://doi.org/10.1039/C1JA10172B

Paton, C., Woodhead, J. D., Hergt, J. M., Phillips, D., & Shee, S. (2007). Strontium isotope analysis of kimberlitic groundmass perovskite via LA-MC-ICP-MS. *Geostandards and Geoanalytical Research*, *31*(4), 321–330. https://doi.org/10.1111/j.1751-908X.2007.00131.x

Pawlig, S., & Baumgartner, L. P. (2001). Geochemistry of a talc-kyanite-chloritoid shear zone within the Monte Rosa granite. *Val d'Ayas, Italy [Text/html,application/pdf,text/html]*. https://doi.org/10.5169/SEALS-61696

Pennacchioni, G., Ceccato, A., Fioretti, A. M., Mazzoli, C., Zorzi, F., & Ferretti, P. (2016). Episyenites in meta-granitoids of the Tauern Window (Eastern Alps): Unpredictable? *Journal of Geodynamics*, *101*, 73–87. https://doi.org/10.1016/j.jog.2016.04.001

Piantelli, F. M., Nibourel, L., Berger, A., & Herwegh, M. (2026). From a Continental Margin to an alpine dome: 4D geodynamic evolution of the AAR massif. *Τεκτονικα*, *4*(1). https://doi.org/10.55575/tektonika2026.4.1.105

Pitzer, K. S., & Sterner, S. M. (1995). Equations of state valid continuously from zero to extreme pressures with H_2O and CO_2 as examples. *International Journal of Thermophysics*, *16*(2), 511–518. https://doi.org/10.1007/BF01441917

Pourmand, A., Dauphas, N., & Ireland, T. J. (2012). A novel extraction chromatography and MC-ICP-MS technique for rapid analysis of REE, Sc and Y: Revising CI-chondrite and Post-Archean Australian Shale (PAAS) abundances. *Chemical Geology*, *291*, 38–54. https://doi.org/10.1016/j.chemgeo.2011.08.011

Pradhan, S., & Sen, I. S. (2024). Metamorphic CO_2 fluxes offset the net geological carbon sink in the Himalayan-Tibetan orogen. *Earth and Planetary Science Letters*, *647*, 119018. https://doi.org/10.1016/j.epsl.2024.119018

Rast, M., Galli, A., Ruh, J. B., Guillong, M., & Madonna, C. (2022). Geology along the Bedretto tunnel: Kinematic and geochronological constraints on the evolution of the Gotthard Massif (Central Alps). *Swiss Journal of Geosciences*, *115*(1), 8. https://doi.org/10.1186/s00015-022-00409-w

Rauchenstein-Martinek, K., Wagner, T., Wälle, M., Heinrich, C. A., & Arlt, T. (2016). Chemical evolution of metamorphic fluids in the Central Alps, Switzerland: Insight from LA-ICPMS analysis of fluid inclusions. *Geofluids*, *16*(5), 877–908. https://doi.org/10.1111/gfl.12194

Rawat, G., Arora, B. R., & Gupta, P. K. (2014). Electrical resistivity cross-section across the Garhwal Himalaya: Proxy to fluid-seismicity linkage. *Tectonophysics*, *637*, 68–79. https://doi.org/10.1016/j.tecto.2014.09.015

Robert, F., Boullier, A. M., & Firdaous, K. (1995). Gold-quartz veins in metamorphic terranes and their bearing on the role of fluids in faulting. *Journal of Geophysical Research*, *100*(B7), 12861–12879. https://doi.org/10.1029/95JB00190

Roberts, N. M. W., Rasbury, E. T., Parrish, R. R., Smith, C. J., Horstwood, M. S. A., & Condon, D. J. (2017). A calcite reference material for LA-ICP-MS U-Pb geochronology. *Geochemistry, Geophysics, Geosystems*, *18*(7), 2807–2814. https://doi.org/10.1002/2016GC006784

Rolland, Y., & Rossi, M. (2016). Two-stage fluid flow and element transfers in shear zones during collision burial-exhumation cycle: Insights from the Mont Blanc Crystalline Massif (Western Alps). *Journal of Geodynamics*, *101*, 88–108. https://doi.org/10.1016/j.jog.2016.03.016

Rolland, Y., Rossi, M., Cox, S. F., Corsini, M., Mancktelow, N., Pennacchioni, G., et al. (2008). $^{40}Ar/^{39}Ar$ dating of synkinematic white mica: Insights from fluid-rock reaction in low-grade shear zones (Mont Blanc Massif) and constraints on timing of deformation in the NW external Alps. *Geological Society Special Publication*, *299*(1), 293–315. https://doi.org/10.1144/SP299.18

Rossi, M., & Rolland, Y. (2014). Stable isotope and Ar/Ar evidence of prolonged multiscale fluid flow during exhumation of orogenic crust: Example from the Mont Blanc and Aar Massifs (NW Alps). *Tectonics*, *33*(9), 1681–1709. https://doi.org/10.1002/2013TC003438

Rovetta, M. R., Blacic, J. D., & Delaney, J. R. (1987). Microfracture and crack healing in experimentally deformed peridotite. *Journal of Geophysical Research*, *92*(B12), 12902–12910. https://doi.org/10.1029/JB092iB12p12902

Rowe, C. D., Kirkpatrick, J. D., & Brodsky, E. E. (2012). Fault rock injections record paleo-earthquakes. *Earth and Planetary Science Letters*, *335–336*, 154–166. https://doi.org/10.1016/j.epsl.2012.04.015

Sharp, Z. D. (2005). Stable isotope geochemistry and formation mechanisms of quartz veins; extreme paleoaltitudes of the Central Alps in the Neogene. *American Journal of Science*, *305*(3), 187–219. https://doi.org/10.2475/ajs.305.3.187

Sibson, R. H. (1990). Conditions for fault-valve behavior. *Geological Society, London, Special Publications*, *54*(1), 15–28. https://doi.org/10.1144/GSL.SP.1990.054.01.02

Simmons, S. F., & Christenson, B. W. (1994). Origins of calcite in a boiling geothermal system. *American Journal of Science*, *294*, 3–400. https://doi.org/10.2475/ajs.294.3.361

Sørensen, B. E., Grant, T., Ryan, E. J., & Larsen, R. B. (2019). In situ evidence of earthquakes near the crust mantle boundary initiated by mantle CO_2 fluxing and reaction-driven strain softening. *Earth and Planetary Science Letters*, *524*, 115713. https://doi.org/10.1016/j.epsl.2019.115713

Tamburello, G., Pondrelli, S., Chiodini, G., & Rouwet, D. (2018). Global-scale control of extensional tectonics on CO_2 Earth degassing. *Nature Communications*, *9*(1), 4608. https://doi.org/10.1038/s41467-018-07087-z

Tarantola, A., Mullis, J., Guillaume, D., Dubessy, J., de Capitani, C., & Abdelmoula, M. (2009). Oxidation of CH_4 to CO_2 and H_2O by chloritization of detrital biotite at 270 ± 5°C in the external part of the Central Alps, Switzerland. *Lithos*, *112*(3–4), 497–510. https://doi.org/10.1016/j.lithos.2009.04.008

Tarantola, A., Mullis, J., Vennemann, T., Dubessy, J., & De Capitani, C. (2007). Oxidation of methane at the CH_4/H_2O–(CO_2) transition zone in the external part of the Central Alps, Switzerland: Evidence from stable isotope investigations. *Chemical Geology*, *237*(3–4), 329–357. https://doi.org/10.1016/j.chemgeo.2006.07.007

15252027, 2026, 11, Downloaded from https://agupubs.onlinelibrary.wiley.com/doi/10.1029/2026GC013384 by CochraneItalia, Wiley Online Library on [17/11/2026]. See the Terms and Conditions (https://onlinelibrary.wiley.com/terms-and-conditions) on Wiley Online Library for rules of use; OA articles are governed by the applicable Creative Commons License

Tavazzani, L., Guillong, M., Giuliani, A., Fontboté, L., & Chelle-Michou, C. (2024). Not so fast: Million-years of metal precipitation in Mississippi Valley type deposits inferred from in-situ petrochronology of hydrothermal carbonates. *Earth and Planetary Science Letters*, *636*, 118718. https://doi.org/10.1016/j.epsl.2024.118718

Taylor, B. E., & Bucher-Nurminen, K. (1986). Oxygen and carbon isotope and cation geochemistry of metasomatic carbonates and fluids—Bergell aureole, Northern Italy. *Geochimica et Cosmochimica Acta*, *50*(6), 1267–1279. https://doi.org/10.1016/0016-7037(86)90410-2

Todd, C. S., & Engi, M. (1997). Metamorphic field gradients in the Central Alps. *Journal of Metamorphic Geology*, *15*(4), 513–530. https://doi.org/10.1111/J.1525-1314.1997.00038.X

Trommsdorff, V., & Skippen, G. (1986). Vapour loss ("boiling") as a mechanism for fluid evolution in metamorphic rocks. *Contributions to Mineralogy and Petrology*, *94*(3), 317–322. https://doi.org/10.1007/BF00371440

Uysal, I. T., Zhao, J. X., Golding, S. D., Lawrence, M. G., Glikson, M., & Collerson, K. D. (2007). Sm–Nd dating and rare-Earth element tracing of calcite: Implications for fluid-flow events in the Bowen Basin, Australia. *Chemical Geology*, *238*(1–2), 63–71. https://doi.org/10.1016/j.chemgeo.2006.10.014

Wang, P., Wang, B., Peng, Z., & Lei, X. (2026). Reactivation of basement faults by deep fluids during the 2017 Changdao earthquake swarm, Eastern China. *Communications Earth & Environment*, *7*(1), 207. https://doi.org/10.1038/s43247-026-03228-1

Watson, B. E., & Brenan, J. M. (1987). Fluids in the lithosphere, 1. Experimentally-determined wetting characteristics of CO_2-H_2O fluids and their implications for fluid transport, host-rock physical properties, and fluid inclusion formation. *Earth and Planetary Science Letters*, *85*(4), 497–515. https://doi.org/10.1016/0012-821X(87)90144-0

Weatherley, D. K., & Henley, R. W. (2013). Flash vaporization during earthquakes evidenced by gold deposits. *Nature Geoscience*, *6*(4), 294–298. https://doi.org/10.1038/ngeo1759

Williams, R. T. (2019). Coseismic boiling cannot seal faults: Implications for the seismic cycle. *Geology*, *47*(5), 461–464. https://doi.org/10.1130/G45936.1

Williams, R. T., Beard, B. L., Goodwin, L. B., Sharp, W. D., Johnson, C. M., & Mozley, P. S. (2019). Radiogenic isotopes record a 'drop in a bucket'–A fingerprint of multi-kilometer-scale fluid pathways inferred to drive fault-valve behavior. *Journal of Structural Geology*, *125*, 262–269. https://doi.org/10.1016/j.jsg.2018.07.023

Williams, R. T., & Fagereng, Å. (2022). The role of quartz cementation in the seismic cycle: A critical review. *Reviews of Geophysics*, *60*(1), e2021RG000768. https://doi.org/10.1029/2021RG000768

Woodcock, N. H., Dickson, J. A. D., & Tarasewics, J. P. T. (2007). Transient permeability and reseal hardening in fault zones: Evidence from dilation breccia textures. *Geological Society Special Publication*, *270*, 43–53. https://doi.org/10.1144/GSL.SP.2007.270.01.03

Woodhead, J., Swearer, S., Hergt, J., & Maas, R. (2005). In situ Sr-isotope analysis of carbonates by LA-MC-ICP-MS: Interference corrections, high spatial resolution and an example from otolith studies. *Journal of Analytical Atomic Spectrometry*, *20*(1), 22–27. https://doi.org/10.1039/B412730G

References From the Supporting Information

Baggio, P., & Mezzacasa, G. (1971). *Carta geologica della zona tra la Brenva e T. Jetoula (Massiccio del Monte Bianco)*. STEM Mucchi. [Map].

Ma, X., Wang, G., Hu, D., Liu, Y., Zhou, H., & Liu, F. (2020). Mechanical properties of granite under real-time high temperature and three-dimensional stress. *International Journal of Rock Mechanics and Mining Sciences*, *136*, 104521. https://doi.org/10.1016/J.IJRMMS.2020.104521

Rolland, Y., Cox, S. F., & Corsini, M. (2009). Constraining deformation stages in brittle-ductile shear zones from combined field mapping and $^{40}Ar/^{39}Ar$ dating: The structural evolution of the Grimsel Pass area (Aar Massif, Swiss Alps). *Journal of Structural Geology*, *31*(11), 1377–1394. https://doi.org/10.1016/j.jsg.2009.08.003

Rosenbaum, G., & Lister, G. S. (2005). The Western Alps from the Jurassic to Oligocene: Spatio-temporal constraints and evolutionary reconstructions. *Earth-Science Reviews*, *69*(3), 281–306. https://doi.org/10.1016/j.earscirev.2004.10.001

Wehrens, P., Berger, A., Peters, M., Spillmann, T., & Herwegh, M. (2016). Deformation at the frictional-viscous transition: Evidence for cycles of fluid-assisted embrittlement and ductile deformation in the granitoid crust. *Tectonophysics*, *693*, 66–84. https://doi.org/10.1016/j.tecto.2016.10.022

Wehrens, P., Baumberger, R., Berger, A., & Herwegh, M. (2017). How is strain localized in a meta-granitoid, mid-crustal basement section? Spatial distribution of deformation in the central Aar massif (Switzerland). *Journal of Structural Geology*, *94*, 47–67. https://doi.org/10.1016/j.jsg.2016.11.004

15252027, 2026, 11, Downloaded from https://agupubs.onlinelibrary.wiley.com/doi/10.1029/2026GC013384 by CochraneItalia, Wiley Online Library on [17/11/2026]. See the Terms and Conditions (https://onlinelibrary.wiley.com/terms-and-conditions) on Wiley Online Library for rules of use; OA articles are governed by the applicable Creative Commons License